

An Attempt To Measure The Time Delays Of Three Gravitational Lenses

by

Gheorghe Chistol

Submitted to the Department of Physics
in partial fulfillment of the requirements for the degree of

Bachelor of Science in Physics

at the

MASSACHUSETTS INSTITUTE OF TECHNOLOGY

May 2007

[June 2007]

© Gheorghe Chistol, MMVII. All rights reserved.

The author hereby grants to MIT permission to reproduce and
distribute publicly paper and electronic copies of this thesis document
in whole or in part.

Author

Department of Physics

May 11, 2007

Certified by.....

Joshua N. Winn

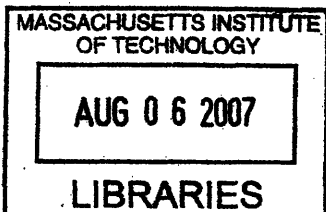
Assistant Professor of Physics

Thesis Supervisor

Accepted by

David E. Pritchard

Cecil and Ida Green Professor of Physics



ARCHIVES

An Attempt To Measure The Time Delays Of Three Gravitational Lenses

by

Gheorghe Chistol

Submitted to the Department of Physics
on May 11, 2007, in partial fulfillment of the
requirements for the degree of
Bachelor of Science in Physics

Abstract

I present the results of reduction and analysis of two seasons of gravitational lens monitoring using the Very Large Array (VLA) at 8.5 GHz. The campaign monitored five gravitational lenses, GL1608, GL1830, GL1632, GL1838, and GL2004 from 24 January 2002 until 18 September 2002, and from 21 May 2003 until 29 January 2004. In addition to gravitational lenses, the campaign monitored ten flux and phase calibrators.

The goal of this work was to measure the gravitational lens time delays. The ultimate goal was to estimate H_0 in a one-step calculation as proposed by Refsdal in 1964 [30]. I reduced the data using AIPS and DIFMAP astronomical data processing software. I analyzed the final light curves in MATLAB using Pelt's non-interpolative dispersion method [33]. Monte Carlo simulations were used to verify the results. I focused my analysis on three lenses: GL1632, GL1838, and GL2004.

Two gravitational lenses, GL1632, and GL1838 exhibited significant flux variability and I was able to measure tentative time delay for these lenses. My analysis suggests a time delay of $\tau_{GL1632} = 182_{-30}^{+8}$ days. I used this value and the lens model by Winn et al. [15] to calculate $H_0 = 65.1_{-2.7}^{+12.9}$ km sec⁻¹ Mpc⁻¹ for a flat cosmological model with $\Omega_m = 0.3$, $\Omega_\Lambda = 0.7$.

For GL1838, I calculated a tentative time delay of $\tau_{GL1838} = 35 \pm 5$ days. Combined with Winn's lens model, this tentative measurement gives $H_0 = 42.6_{-5.3}^{+5.1}$ km sec⁻¹ Mpc⁻¹ (for $\Omega_m = 0.3$, $\Omega_\Lambda = 0.7$). Unfortunately the GL1838 time delay calculation was based on a light curve feature at the end of Season 2 and is not very reliable.

The flux density of GL2004 images varied very little over the course of the campaign and it was not possible to calculate its time delay. However, we observed an interesting pattern of variability in light curves suggesting that GL2004 is probably subject to differential Galactic scintillation.

Our observations show that GL1838 and GL1632 experience significant flux density variations on timescales of months, so it should be possible to measure their time delay more accurately in future monitoring campaigns.

23V11051A

Thesis Supervisor: Joshua N. Winn
Title: Assistant Professor of Physics

Acknowledgments

I want to thank my Thesis Supervisor, Professor Joshua N. Winn, for guiding me through this research project. Prof. Winn provided me with the raw observation data, sample AIPS and DIFMAP scripts. He also taught me the basics of AIPS and DIFMAP. I especially want to thank him for letting me work at my own pace.

I am very grateful to Ojog Constantin, Ojog Svetlana, Ojog Mihai, and Ojog Alexandru, for being a family to me. I would also like to thank them for supporting my studies abroad. If it were not for the Ojogs, I would not be at MIT

I want to thank Radu Berinde for suggesting using VMWare Virtual Machines and helping me set them up.

Many thanks to my friends at Technique, The Yearbook of MIT, for helping me forget about school when that was needed.

Contents

1	Introduction	13
1.1	Motivation and Background	13
1.1.1	What is a Gravitational Lens?	14
1.1.2	QSO 0957+561 - The First Measured Time Delay	15
1.2	Why Measure H_0 the Refsdal Way?	16
1.3	Meet our Lenses	17
1.3.1	CLASS B1608+656 Gravitational Lens	17
1.3.2	PMN J1632-0033 Gravitational Lens	19
1.3.3	PKS 1830-211 Gravitational Lens	20
1.3.4	PMN J1838-3427 Gravitational Lens	22
1.3.5	PMN J2004-1349 Gravitational Lens	23
2	Radio Interferometry	27
2.1	Observing an Astronomic Source	28
2.2	Synthesis Imaging	29
2.3	Radio Antennas and Data Acquisition	30
2.4	Coordinate Systems in Radio Interferometry	31
2.5	Synthesis Array Design	32
3	Observations	34
3.1	Campaign Scheduling	34
3.2	Observation Layout	34

4	Data Reduction	37
4.1	Initial Flagging in AIPS	38
4.2	Calibration in AIPS	39
4.2.1	Primary Flux Calibration	40
4.2.2	AIPS File Management	41
4.3	Data Reduction in DIFMAP	41
4.3.1	Flagging Gravitational Lens Data in DIFMAP	41
4.3.2	Source Model Fitting in DIFMAP	42
5	Light Curves	45
5.1	Raw Light Curves for Calibrators	45
5.2	Light Curve Editing	49
5.3	Residual Map RMS vs Expected Map RMS	50
5.4	Secondary Flux Calibration	51
5.4.1	Gain Elevation Effect and Secondary Calibration	51
6	Time Delay Measurements	55
6.1	Final Light Curves for Gravitational Lenses	55
6.2	Measuring The Time Delays	58
6.3	Error Estimation	59
6.4	Pelt's Dispersion Method	60
6.5	Searching the Parameter Space	63
6.6	Simulations	65
6.6.1	Code Testing on GL1608 Data from Fassnacht et al.	66
6.7	Simulation Results	68
6.7.1	GL1632	68
6.7.2	GL1838	69
6.7.3	GL2004	70
7	Conclusions	80
7.1	What Could Have Been Done Differently	82

7.2	Future Work	83
A	AIPS and DIFMAP Scripts	84
A.1	"Do-It-All" AIPS Script	84
A.2	DIFMAP Script for Fitting GL Data	91
A.3	Bash Script for Screening Calibrators in DIFMAP	93
A.4	Bash Script for Flagging GLs in DIFMAP	94

List of Figures

1-1	GL1608: Clean Map by Fassnacht et al. [8]. X-band (8.5 GHz) VLA Data.	18
1-2	GL1632: Clean Maps by Winn et al. [15]	20
1-3	GL1830: Clean Map Obtained with MERLIN at 5GHz by Lovell et al. Image taken from http://www.atnf.csiro.au/people/jlovell/1830-211/	21
1-4	GL1838: Clean Maps by Winn et al. [16]	25
1-5	GL2004: Clean Maps by Winn et al. [13]	26
2-1	The coordinate system used for interferometer baselines. Figure scanned from page 20 of [1].	31
2-2	a) The configuration of the VLA with its 27 antennas. b) Examples of VLA (u, v) coverage for different declinations. The observation durations were: $\pm 4^h$ for $\delta = 0^\circ$; $\pm 4^h$ for $\delta = 45^\circ$; $\pm 3^h$ for $\delta = -30^\circ$; $\pm 5^m$ for the snapshot at Zenith. Figure scanned from page 30 of [1].	33
5-1	1400+621: Initial light curve.	46
5-2	1545+478: Initial light curve.	46
5-3	1634+627: Initial light curve. Note that this source was observed only during Season 1.	46
5-4	1642+689: Initial light curve. Note that this source was observed only during Season 1.	47
5-5	1651+014: Initial light curve.	47
5-6	1734+094: Initial light curve.	47
5-7	1820-254: Initial light curve.	48

5-8	2011-157: Initial light curve.	48
5-9	2130+050: Initial light curve.	48
5-10	2355+498: Initial light curve.	49
5-11	Gain Elevation Effects for Season 1 and Season 2 respectively.	52
5-12	Gain Elevation Effect Correction for Season 1. Note how the secondary flux calibration cancels out the gain elevation effect and reduces the scatter in the light curves.	52
5-13	Secondary Calibration Gain plot for Season 1 Data	53
6-1	GL1608: Final light curves. Fractional flux variations are the same for all subplots. Residual map RMS is comparable to the symbol size on the plot.	56
6-2	GL1830: Final light curves. Fractional flux variations are the same in both subplots. Residual map RMS is smaller than the symbol size on the plot. Note that the dotted vertical lines denote the VLA configuration changes. In order, from left to right: D- ζ A, A- ζ BnA, BnA- ζ B, B- ζ C, [break], D- ζ A, A- ζ BnA, BnA- ζ B, B- ζ C.	57
6-3	GL1632: Final light curves. Fractional flux variations are the same for images A and B. Residual map RMS is smaller than the symbol size on the plot.	57
6-4	GL1838: Final light curves. Fractional flux variations are the same for images A and B. Note that the light curve of Image B is considerably noisier than that of Image A.	58
6-5	GL2004: Final light curves. Fractional flux variations are the same on both plots. Note that Image A is considerable noisier than Image B.	58
6-6	Creating a combined light curve (b) using raw light curves from (a). The first curve (solid circles) was left unchanged, while the second curve (empty circles) was magnified by a factor of M=2 and shifted forward in time by 50 days.	61

6-7	GL1608: Season 1 Light Curves of Images A and B from Fassnacht et al. [7]. The fractional flux variations are the same on both plots. . . .	67
6-8	GL1608: Season 1 Smoothed Light Curves if Images A and B. Fractional flux variations are the same on both plots.	67
6-9	GL1608: The results of 10000 simulations using Fassnacht's data from Season 1 [7]. The simulated light curves were generated as described in the Simulation subsection. The calculated time delay is $\tau_{AB} = -30^{+4}_{-7.5}$ days (68% confidence interval). This time delay is negative because image B leads image A. This is in good agreement with the result $\tau_{AB} = -31^{+3}_{-2}$ days (68% confidence interval) calculated by Fassnacht using the same data. Note that Fassnacht used different smoothing filters and a somewhat different Monte Carlo procedure.	72
6-10	GL1608: Dispersion plot for Fassnacht's Season 1 data. Quadratic weighting was used to calculate D_1^2 dispersion.	72
6-11	GL1608: Combined Final Light-Curve. Based on Fassnacht's data and parameters calculated by my code.	73
6-12	GL1632: Smoothed light curves. Fractional flux variations are the same in both images.	74
6-13	GL1632: Histogram showing the results of 10000 simulations. This histogram suggests a tentative time delay $\tau_{AB} = 156^{+38}_{-70}$ days. Note that this is a very conservative estimate.	75
6-14	GL1632: Dispersion curve for optimal fit parameters. $M_1 = 12.156$ and $M_2 = 11.340$ are the best-fit magnification ratios for Seasons 1 and 2.	75
6-15	GL1632: Combined Light Curve for $M_1=12.156$ and $M_2=11.340$ and a time delay of $\tau_{AB} = 182$ days, corresponding to the minimum in the Pelt Dispersion plot form Figure 6-14	76

6-16	GL1632: Window function versus trial time delays. The window function value corresponds to the number of pairs of points contributing to the dispersion calculation. As the trial time delay increases, the curves are shifted more with respect to each other, the overlap between light curves of A and B decreases, and the window function value goes down.	76
6-17	GL1838: Smoothed light curves. Fractional flux variations are the same for images A and B. Note that the light curve of image B is much noisier than that of image A.	77
6-18	GL1838: Plot of Pelt D_1^2 dispersion as a function of trial time delays (all light-curve points were weighted uniformly). This plot suggests a time delay $\tau_{AB} = 40$ days. The best fit magnification ratios are $M_1=13.68$, and $M_2=14.04$ for Seasons 1 and 2 respectively. See Figure 6-19 for the combined light curves.	78
6-19	GL1838: Combined light curves for $M_1=13.68$, $M_2=14.04$, and $\tau_{AB} = 40$ days.	78
6-20	GL2004: Smoothed light curves. Fractional flux variations are the same on both plots. Note that the light curve of image A is much noisier than that of image B.	79
6-21	GL2004: Histogram showing the results of 10000 simulations. Pelt's method failed to measure the time delay of GL2004.	79

List of Tables

3.1	The number of epochs when various sources were observed. Sometimes a particular source was not visible to the VLA at the time of observation. The top section contains the gravitational lens data, the middle section contains statistics about flux calibrators, and the bottom section of the table contains phase calibrator statistics.	35
3.2	Phase Calibrators Associated with Each Gravitational Lens	36
4.1	Source Parameters used by DIFMAP model-fitting scripts. Flux Density was the only free parameter. The second column contains initial value guesses for the flux density. *Note that 1634+627 was modeled as an Elliptical Gaussian Function, whereas all the other calibrators were modeled as point sources.	44

Chapter 1

Introduction

Gravitational lensing is a consequence of General Relativity. A massive body curves space-time in its vicinity and light rays are bent by its gravity. The first instance of gravitational lensing was observed during a solar eclipse in an expedition organized by Eddington in 1919 [5]. This was the first piece of evidence to support General Relativity.

Einstein predicted that single stars could act like lenses by deflecting light in their gravitational field [2]. Given the small mass of a star, Einstein remarked that it would be almost impossible to observe a single-star lens due to the small angular separation between images [2]. It was Zwicky in 1937 who suggested that galaxies could act as gravitational lenses, and that galactic masses could be much larger than originally thought [24], [25]. In this case, reasoned Zwicky, gravitational lens images could be resolved by optical telescopes on Earth. Zwicky also predicted that gravitational lensing could be used to observe very faint distant galaxies [24].

1.1 Motivation and Background

Einstein's theory of General Relativity provided predictions that were considered wild at the time. The idea that our universe might be expanding was very hard to accept in the early 20th century. In 1922, Alexander Friedmann used Einstein's field equations to show that the universe could be expanding [3], something that was

independently confirmed by Georges Lemaitre in 1927 (hence the name “Friedmann-Lemaitre-Robertson-Walker Metric”). In the late 1920s, Edwin Hubble, who was working at the Mount Wilson Observatory, confirmed Friedmann’s hypothesis. Hubble used his own galaxy distance measurements combined with redshift data from the American astronomer Vesto Slipher, to find that the observed velocity of a galaxy is roughly proportional to its distance from Earth [27]. Written in the form of Equation 1.1, this is now known as the Hubble law (here v is the velocity of a galaxy, D is the distance to the galaxy, and H_0 is the rate of expansion, known as the Hubble Constant).

$$v = H_0 D \tag{1.1}$$

Hubble’s analysis based on 46 “nebulae”¹ measurements suggested a value of about 500 km sec⁻¹Mpc⁻¹ for H_0 [27]. Hubble’s original plot of galaxy velocity versus distance contained significant scatter, which is now explained by the fact that in addition to the Hubble flow², galaxies have some local dispersion velocity. Hubble’s initial estimate of H_0 was much larger than the currently accepted value of ~ 70 km sec⁻¹Mpc⁻¹ because of significant calibration errors in his distance measurements.

1.1.1 What is a Gravitational Lens?

In a revolutionary paper published in 1964, Sjur Refsdal described how the Hubble constant could be calculated from the time delays of gravitational lenses [30]. A massive body, such as a star or a galaxy, can act as a lens to form multiple images of a background object. Confusion might arise when the term “gravitational lens” is used. I will use the terms “lensing galaxy” and “lens images” to refer to the lens itself and its images.

It takes light different amounts of time to reach Earth from two different images formed by a gravitational lens. As a result, intrinsic variations in the background

¹Up until mid-1900’s, astronomers used the term “nebulae” to refer to galaxies. The word “galaxy” entered the lexicon somewhat later.

²Hubble Flow - the large-scale expansion of the universe

source are observed at different times in different images. Refsdal showed that the time delay is proportional to the difference in optical paths, which is proportional to H_0^{-1} [30], [34]. One needs to know the model of the lensing galaxy and the time delay between different images in order to calculate H_0 [4].

The simplest possible model for a lensing galaxy is a singular isothermal sphere. In this case, the formula for the time delay is given by Equation 1.2 [13]. Here $\Delta\theta$ is the angular separation between images A and B; μ is the magnification ratio; z_l is the lens redshift; D_l , D_s , and D_{ls} are the angular diameter distances to the lensing galaxy, to the background source (quasar), and the angular diameter distance between the lensing galaxy and the background source.

$$\Delta t = \frac{1}{2c} \left(\frac{D_l D_s}{D_{ls}} \right) (1 + z_l) (\Delta\theta)^2 \left(\frac{\mu - 1}{\mu + 1} \right) \quad (1.2)$$

In order to achieve good accuracy, one needs to monitor a gravitational lens for a period longer than its time delay. The analysis of light curves³ is complicated by the fact that data is sampled non-uniformly. Sophisticated methods have been devised to cope with this.

1.1.2 QSO 0957+561 - The First Measured Time Delay

Discovered in 1979, QSO 0957+561 was the first lens to be monitored systematically in optical and radio waves [33]. However, the body of data that accumulated over the years suggested two different time delay candidates – $\Delta\tau_1 \approx 1.14$ years and $\Delta\tau_2 \approx 1.48$ years [4]. Various teams of astronomers repeatedly published papers in the early and mid 1990s arguing in favor of the first or the second value. The debate was finally settled favorably for the shorter time delay. This example shows that calculating the time delay is not trivial, even when a large amount of data is available.

In an attempt to resolve the QSO 0957+561 controversy, Pelt et al. devised a simple and robust algorithm for computing time delays from unevenly sampled data without resorting to interpolation methods [33]. Given that data are usually quite

³Light Curve – plot of the flux density versus time.

noisy, any interpolation method is susceptible to noise spikes and could affect the measurement accuracy. I used Pelt's dispersion method to analyze the final light curves from J. N. Winn's monitoring campaign.

1.2 Why Measure H_0 the Refsdal Way?

The Cosmic Distance Ladder is the standard method of measuring Hubble's Constant. Using the parallax method, we can directly measure distances out to only a few hundred parsecs. The classic trick is to use distance indicators and standard candles as intermediate calibrators. Supernovae, Cepheid variable stars, and galaxy clusters are a few examples of distance indicators [4]. Astronomers classified these indicators depending on their magnitude and spectral class. Known standard candles are used as intermediate calibrators to calculate distances to other objects.

Our most accurate measurements of H_0 were made with the Hubble Space Telescope using the Cosmic Distance Ladder method, and have an uncertainty of about 10%. Refsdal's H_0 determination method has a few major advantages over the Cosmic Distance Ladder. First of all, H_0 can be calculated in one step, avoiding the error build-up of the standard method. In addition, one can calculate H_0 using gravitational lenses at large redshifts ($z_l \approx 0.5$) whereas the classical methods observe sources within 100 Mpc or so [4], where local velocities are comparable to the Hubble flow. In addition, the gravitational lensing method is based on fundamental physics (General Relativity) and does not require assumptions about the nature and properties of standard candles.

Of course, Refsdal's method has its drawbacks. There have been only about a dozen confirmed time delay measurements. Even when the time delay of a lens is known with a reasonable accuracy, the lens model is usually overly simplified due to the lack of detailed information about lens position and mass distribution [4]. A large sample of measured time delays is necessary to provide a reliable measurement of H_0 . As the sensitivity of optical telescopes and radio telescopes gets better, astronomers hope to eventually beat the 10% uncertainty on the value of H_0 (as measured with

the Cosmic Distance Ladder) [11]. The current project is a small contribution to this effort.

1.3 Meet our Lenses

This section contains a brief description of each gravitational lens monitored during this campaign. Three of them, PMN J1632-0033, PMN J1838-3427, and PMN J2004-1349, were discovered during a search for lenses in the southern sky by Winn et al. [12], [13], [15]. This search examined a sample of sources in the southern sky ($0^\circ > \delta > -40^\circ$) using the VLA⁴. Lens candidates were later imaged with a variety of radio and optical telescopes, including VLA, VLBA⁵, MERLIN⁶, the Blanco 4m telescope at CTIO⁷, and HST⁸ [12].

1.3.1 CLASS B1608+656 Gravitational Lens

For simplicity, I will refer to the gravitational lenses using the shorthand notation GL****. Also known as GL1608, CLASS B1608+656 has four images, A, B, C, and D, as shown in Figure 1.3.1. This lens was discovered by Myers et al. during a VLA search for radio lenses by the Cosmic Lens All-Sky Survey (CLASS) [21]. GL1608 was re-discovered two months later in an independent survey by Snellen et al. [22]. Myers et al. measured the lensing galaxy redshift $z_l = 0.6304$ via optical spectroscopy with the Palomar 5 m telescope [21]. The background source was identified as a post-starburst galaxy with $z_s = 1.394$ [10].

The flux density ratios for the 4 images are approximately $S_A : S_B : S_C : S_D = 2 : 1 : 1 : 0.35$ [7]. The standard lens model predicts that any flux density variations should be first seen in image B, followed by images A, C, and D (in that order) [7]. GL1608 was the first lens for which all three time delays have been measured.

⁴Very Large Array

⁵Very Long Baseline Array

⁶Multielement Radio-Linked Interferometer Network

⁷Cerro Tololo Inter-American Observatory

⁸Hubble Space Telescope

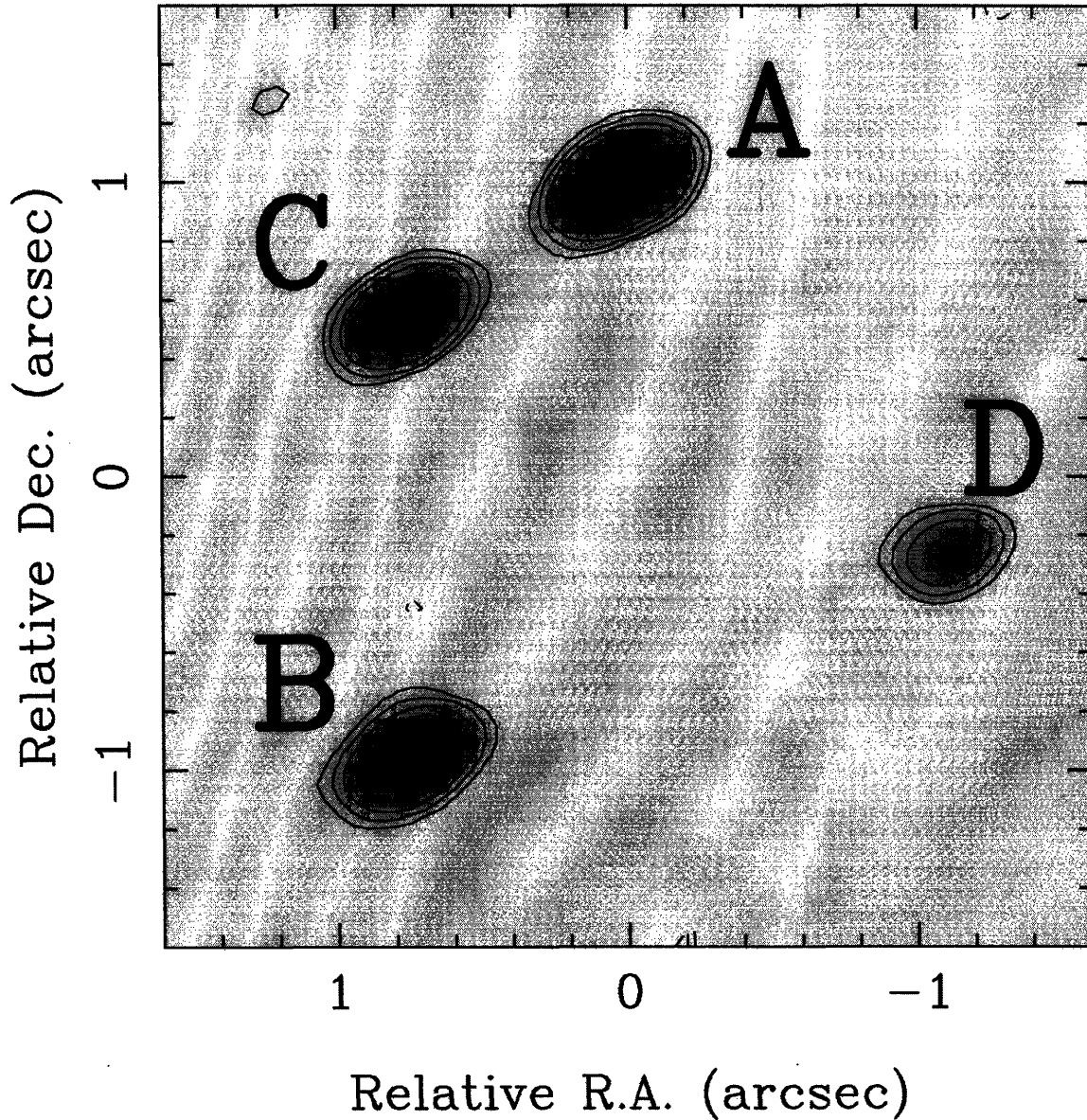


Figure 1-1: GL1608: Clean Map by Fasnacht et al. [8]. X-band (8.5 GHz) VLA Data.

Fasnacht et al. published the results of their first season of GL1608 monitoring in 1999 [7]. Because the features in the light curves had a low amplitude, the time delays were calculated with a large (20%) uncertainty in the 1999 paper.

J. N. Winn included GL1608 in this monitoring campaign hoping to measure the time delays with a better accuracy. However, in late 2002, Fasnacht et al. published a significantly improved time delay measurement for GL1608. Using data from three

seasons of observations, Fassnacht et al. calculated the following GL1608 delays: $\tau_{BA} = 31.5_{-2.5}^{+3.0}$ days, $\tau_{BC} = 36.0_{-2.5}^{+2.5}$ days, $\tau_{BD} = 77.0_{-3.0}^{+4.0}$ days (95% confidence intervals) [8]. These results allowed Fassnacht et al. to calculate $H_0 = 61 - 65$ km $\text{sec}^{-1}\text{Mpc}^{-1}$ for a flat universe with $(\Omega_M, \Omega_\Lambda) = (0.3, 0.7)$ [8]. At this stage the bulk of the uncertainty (± 15 km $\text{sec}^{-1}\text{Mpc}^{-1}$) comes from uncertainties in the lens model. It would be very hard to improve the accuracy of this time delay measurement even further.

After the announcement of Fassnacht’s accurate measurement, Winn decided to drop GL1608 from the rest of his monitoring campaign in order to dedicate more integration time to the remaining sources.

1.3.2 PMN J1632-0033 Gravitational Lens

Winn et al. discovered GL1632 during their search for gravitational lenses in the southern sky [15]. It is a flat spectrum source, suggesting that it should be variable. GL1632 is composed of two main components, A and B, with a flux density ratio of approximately 13:1 at 8.5GHz⁹ [15]. Winn et al. provided evidence for the existence of a much fainter third component, between images A and B [15]. Clean maps of this gravitational lens by Winn et al. are shown in Figure 1.3.2 [15].

The background quasar is situated at a redshift of $z_s = 3.424 \pm 0.007$ [15]. Although the redshift of the lensing galaxy has not been directly measured yet, Winn et al. used Kochanek’s fundamental plane method [18] to estimate $z_l = 1.0 \pm 0.1$ [15]. The isothermal spherical model provides an estimate of about $h\Delta t = 120 - 130$ days¹⁰ for the time delay between GL1632 images [15].

In conclusion, the expected GL1632 time delay is on the order of 10^2 days (component A leading component B). Winn et al. observed mild flux density variability in GL1632 images at 8.5 GHz and the current campaign monitored this lens in an attempt to measure its time delay.

⁹8.5 GHz is the frequency corresponding to the X-band of the VLA. I will often mention this frequency because the current campaign monitored sources in VLA’s X-band.

¹⁰The predicted time delay is expressed as a function of the Hubble constant. Here $h = H_0/100$ km $\text{sec}^{-1}\text{Mpc}^{-1}$.

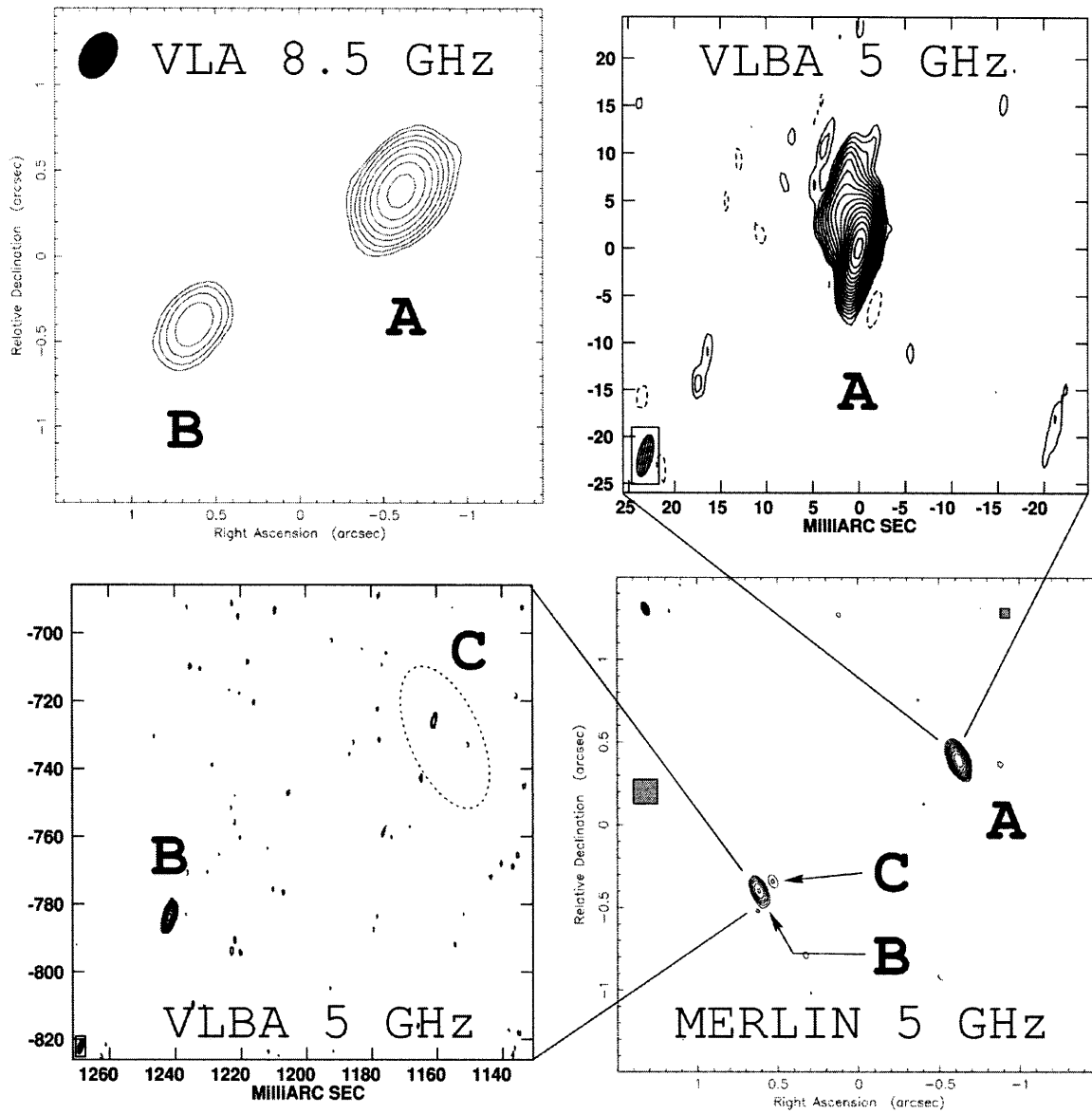


Figure 1-2: GL1632: Clean Maps by Winn et al. [15]

1.3.3 PKS 1830-211 Gravitational Lens

It was Rao and Subrahmanyan in 1988, who first proposed that 1830-211 was a gravitational lens [29]. Jauncey et al. [17] provided final evidence that this was a gravitational lens by identifying its two components. An Einstein ring was found as well (see the GL1830 clean map by Lovell et al. in Figure 1.3.3). In 1999 Lidman et al. used infrared spectroscopy to measure the redshift of the background quasar –

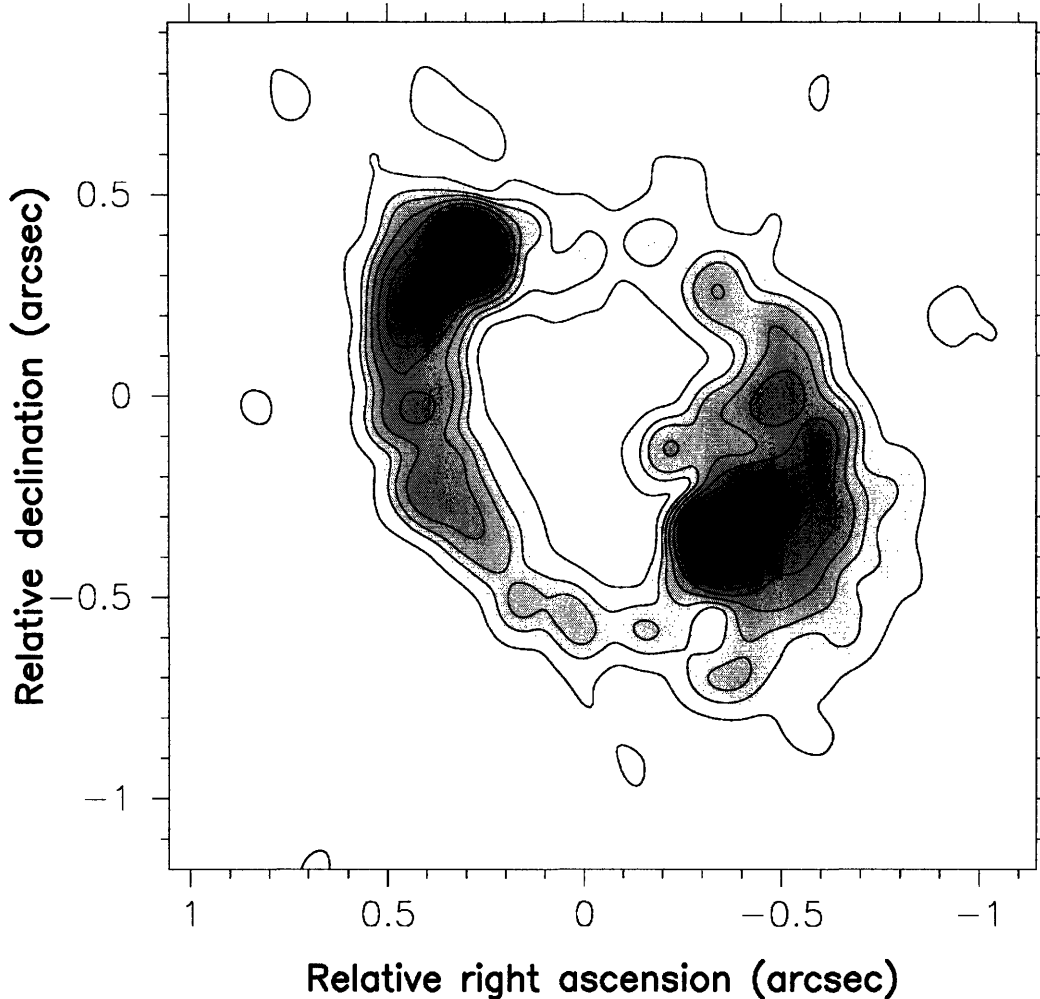


Figure 1-3: GL1830: Clean Map Obtained with MERLIN at 5GHz by Lovell et al. Image taken from <http://www.atnf.csiro.au/people/jlovell/1830-211/>

$z_s = 2.507$ [19].

Throughout late nineties, a few molecular absorption features were identified between the two lens components and they were thought to be the lensing galaxy. Courbin et al. measured the redshift of the lensing galaxy $z_l = 0.886$ [9]. In 2002, Winn et al. published accurate coordinates of the lensing galaxy, based on images from the HST [14].

In 1998 Lovell et. al. measured a time delay of 26^{+4}_{-5} days for this lens [20]. Winn et al. used this result and their own observations of the lensing galaxy to calculate $H_0 = 44 \pm 9 \text{ km sec}^{-1}\text{Mpc}^{-1}$ for a flat cosmological model with $\Omega_m = 0.3$ [14]. This calculation was weakly dependent on the cosmological model, but regardless of the

assumed value for Ω_m , the calculated value for the Hubble constant was significantly lower than the value of $72 \pm 8 \text{ km sec}^{-1}\text{Mpc}^{-1}$ measured with the Distance Ladder method in the Key Project [11].

GL1830 was monitored in this campaign because the original time delay measurement had a 20% uncertainty, and the accuracy of the measurement could be improved. Lovell et al. mentioned that the original light curves were compatible with a wide range of time delays ranging from 12 to 30 days [20]. They finally decided to base their calculation on a subset of the data that contained a distinguishable "bump" in flux density. A time delay calculation based on more than one feature in the light curves is desirable.

1.3.4 PMN J1838-3427 Gravitational Lens

Also known as GL1838 in shorthand notation, this radio-source was identified as a gravitational lens by Winn et al. in 2000 [12]. GL1838 was the first gravitational lens to be discovered in the Southern Sky lens search survey mentioned in the Introduction. The background object is a quasar at redshift $z_s = 2.78$ [12]. The distance to the lensing galaxy could not be measured accurately, but Winn et al. used the fundamental plane method to estimate the lensing galaxy redshift $z_l = 0.36 \pm 0.08$ [12].

Shown in Figure 1.3.4, this lens has two components, A and B, with a flux ratio of approximately 14:1 at 8.5GHz [12]. Winn et al. used a variety of telescopes to obtain the detailed positions and angular dimensions of the lens images and the lens galaxy [12].

Assuming a lens redshift of $z_l = 0.36$ and a quasar redshift of $z_s = 2.78$, Winn et al. predicted an estimated time delay of approximately $h\Delta t = 14 - 15$ (for a flat cosmological model). Image A is expected to lead the fainter image B.

In conclusion, GL1838 has a time delay on the order of 10^1 days, therefore it should be possible to measure it in a monitoring campaign with a sampling interval of 2-3 days. GL1838 has a flat spectral index, which is an indication of intrinsic flux variability.

1.3.5 PMN J2004-1349 Gravitational Lens

The discovery of this lens was announced by Winn et al. in 2001 [13]. Also referred to as GL2004, it was the second lens discovered in the Southern sky search by Winn et al. (the first one being GL1838) [13]. The clean map of GL2004 in Figure 1.3.5 shows that this lens has two images – the NE component (I will refer to it as A) and the SW component (I will refer to it as B).

At 8.5GHz, the flux density ratio of the two components is approximately 1:1, which is somewhat unusual for a gravitational lens [13]. Winn et al. reported that there was no independent evidence for extended emissions from either component of GL2004 [13]. There are no sources in the NVSS¹¹ catalog within 5' of this lens [13] therefore we do not expect any interference from other sources. The spectra of the A and B components are relatively flat, which suggests that the source is intrinsically variable. Winn's summary of radio-observations of GL2004 also suggests that the lens is variable [32].

Assuming $z_s = 2$ and $z_l = 1$, the isothermal sphere model for the lensing galaxy suggests a value $h\Delta t < 3$ days for the time-delay [13]. There are a few complications, for example the fact that an isothermal spherical lens could not theoretically produce two images with exactly equal flux densities.

A follow-up paper by Winn et al. published in November 2003 [32], provided evidence that the lensing galaxy was in fact a spiral galaxy. In 2003, GL2004 was only one of 4 confirmed gravitational lenses whose lensing galaxy was a spiral. This second paper provided additional constraints to the model and more accurate measurements of the lens position (using HST data). Winn et al. suggested that sensitive radio observations could eventually detect a third, very faint, image of the background quasar, or some extended jet component, which could be used to further constrain the lens model [32].

Since the lensing galaxy is a spiral, the expected time delay could be larger than the 3-day estimate provided by Winn et al. in their 2001 GL2004 paper [13]. GL2004 was monitored in this campaign with the intention to measure its time delay. In

¹¹National Radio Astronomy Observatory (NRAO) VLA Sky Survey catalog

addition to a single step Hubble constant calculation, the time delay of GL2004 could be used to infer information about the mass distribution of its lensing galaxy.

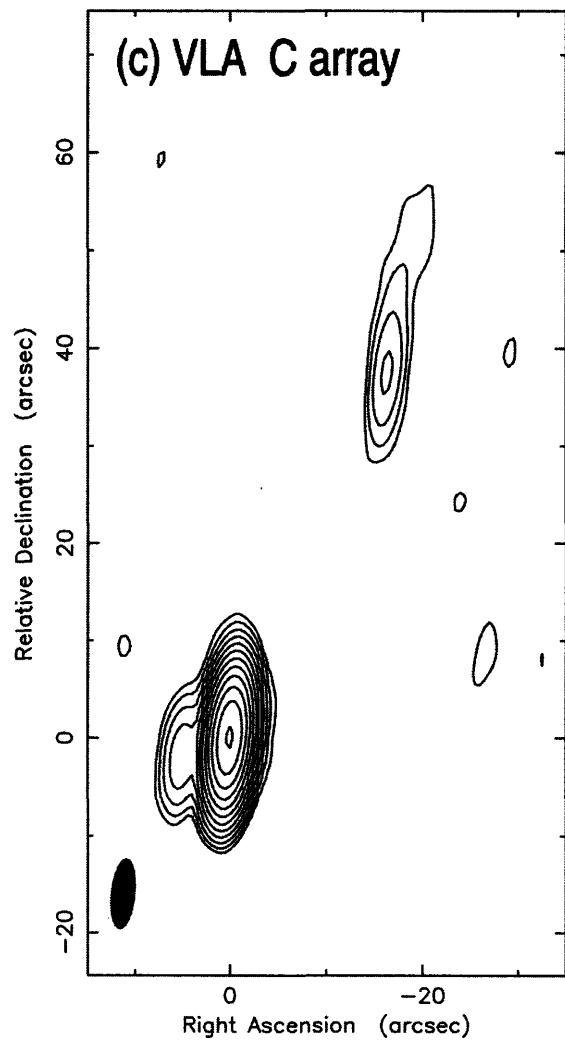
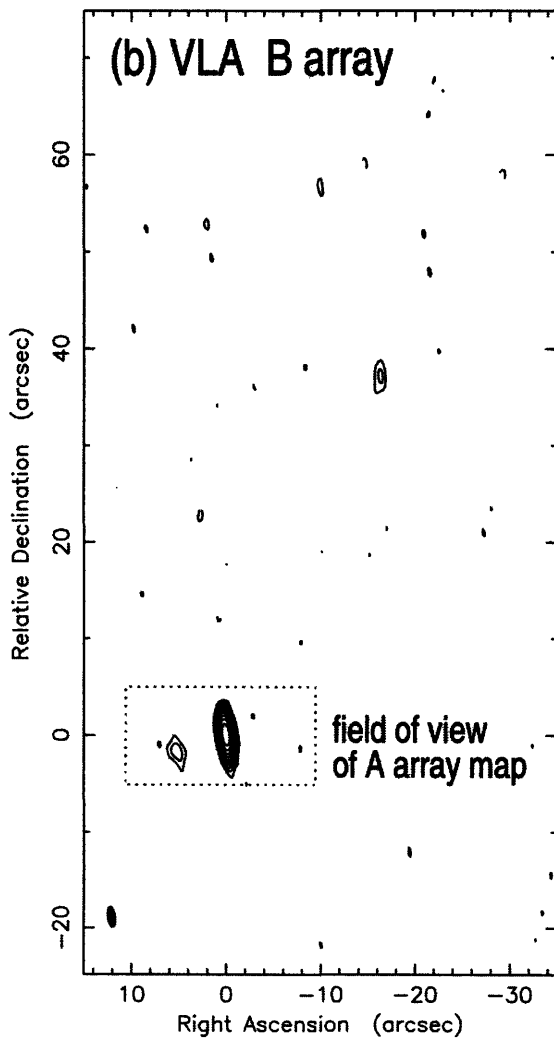
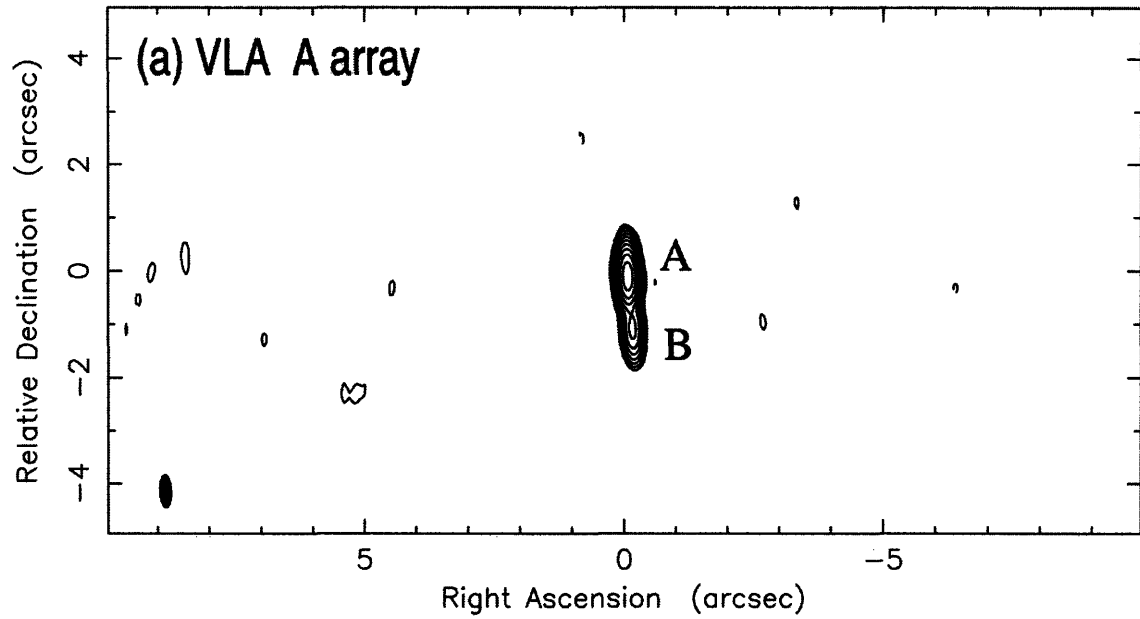


Figure 1-4: GL1838: Clean Maps by Winn et al. [16]

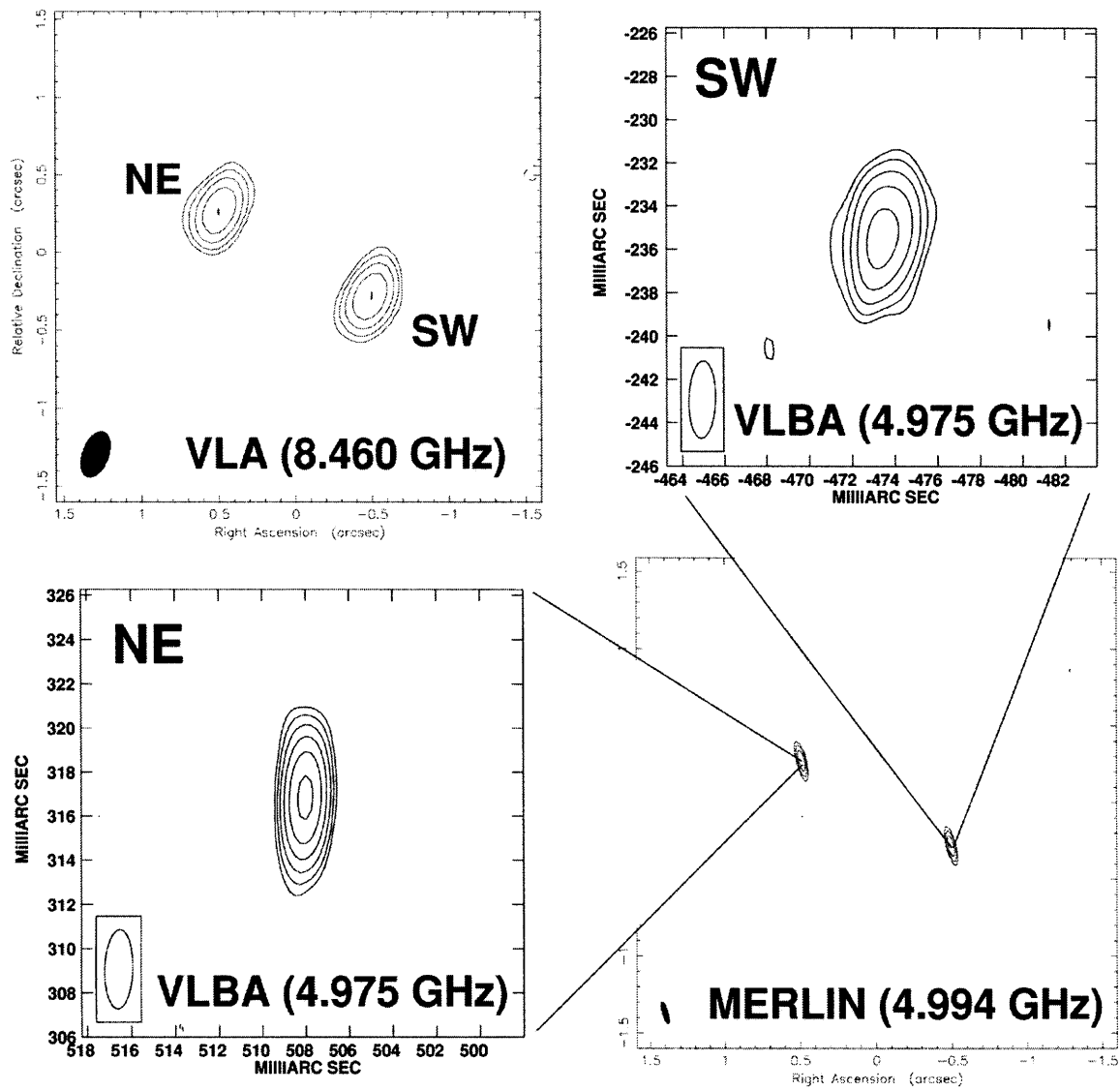


Figure 1-5: GL2004: Clean Maps by Winn et al. [13]

Chapter 2

Radio Interferometry

This is a very brief introduction to the fundamental principles of radio interferometry. Familiarity with the basic concepts will prove useful for understanding this document since I spent a considerable amount of time processing interferometry data.

The idea of using several small antennas/receivers instead of a single large antenna was a result of cost-benefit analysis. The smallest angular dimension φ that can be resolved by a telescope of diameter D at wavelength λ is limited by diffraction: $\varphi \approx \lambda/D$. In order to resolve a small source on the sky, one needs a very large antenna. The Arecibo radio-telescope, the largest on Earth, is 300 meters in diameter. Gigantic radio-telescopes are prohibitively expensive, and are less flexible than smaller antennas. For example you can point a single small parabolic antenna almost anywhere in the sky, whereas the Arecibo telescope has a limited field of view. Synthesis arrays have the advantage of high angular resolution (the individual antennas can be placed far apart), configuration flexibility (individual antennas can be moved to a new location), and cost-efficiency (it is cheaper to manufacture many small radio-antennas than it is to manufacture a single gigantic telescope). The main drawback of a synthesis array is that it has a much lower sensitivity when compared to a single huge antenna. Even though a radio-telescope array has a large resolving power, it has a very small photon collecting area, therefore, it has a low sensitivity.

2.1 Observing an Astronomic Source

Radio-telescopes are antennas that receive electromagnetic waves from distant cosmic objects. Suppose that an antenna at radius-vector position \mathbf{r} is observing a phenomenon/object located with radius-vector \mathbf{R} . The observer records the electric field $\mathbf{E}(\mathbf{R},t)$ that propagates from the source. The field $\mathbf{E}(\mathbf{R},t)$ is characterized by its magnitude and phase. For simplicity and completeness, $\mathbf{E}(\mathbf{R},t)$ will be considered complex. The electromagnetic field is composed of quasi-monochromatic components $\mathbf{E}_\nu(\mathbf{R}, t)$. In general, astronomical sources are very far away, so they can only be described as two-dimensional emitting regions, i.e. the three-dimensional structure is simply projected on the surface of a sphere with radius \mathbf{R} . The observer can only measure the surface brightness distribution on the sky (see Equation 2.1) [1].

$$\mathbf{E}_\nu(\mathbf{r}) = \int \xi_\nu(\mathbf{R}) \frac{e^{2\pi i \nu |\mathbf{R}-\mathbf{r}|/c}}{|\mathbf{R}-\mathbf{r}|} dS \quad (2.1)$$

Here $\xi_\nu(\mathbf{R})$ is the electric field distribution on a celestial sphere of radius \mathbf{R} , and dS is a surface area element on this sphere. Equation 2.1 is valid if the observed astronomical object is very far away, much further than B^2/λ , where $B = |\mathbf{r}_2 - \mathbf{r}_1|$ is the telescope baseline length and λ is the wavelength of electromagnetic radiation [1]. In this context, we assume that there are more than one antennas (the baseline is the distance between two antennas). For two antennas at radius-vectors \mathbf{r}_1 and \mathbf{r}_2 , the correlation of the field at these points is given by Equation 2.2 (the star denotes a complex conjugate).

$$V_\nu(\mathbf{r}_1, \mathbf{r}_2) = \langle \mathbf{E}_\nu(\mathbf{r}_1) \mathbf{E}_\nu^*(\mathbf{r}_2) \rangle \quad (2.2)$$

The final expression for the spatial coherence (or spatial autocorrelation) function is given in Equation 2.3.

$$V_\nu(\mathbf{r}_1, \mathbf{r}_2) \approx \int I_\nu(\mathbf{s}) e^{-2\pi i \nu \mathbf{s} \cdot (\mathbf{r}_2 - \mathbf{r}_1)/c} d\Omega \quad (2.3)$$

Here $\mathbf{s} = \mathbf{R}/|\mathbf{R}|$ is a unit vector and $I_\nu(\mathbf{s}) = |\mathbf{R}|^2 \langle |\xi_\nu(\mathbf{s})|^2 \rangle$ is the observed inten-

sity [1]. Radio astronomers measure the spatial coherence function $V_\nu(\mathbf{r}_1, \mathbf{r}_2)$ using interferometers – arrays of antennas arranged in a certain pattern.

2.2 Synthesis Imaging

Using certain approximations and reasonable assumptions, Equation 2.3 can be inverted to calculate the intensity $I_\nu(\mathbf{s})$. Given two antennas, as shown in Figure 2.4, it is convenient to express their baseline (distance between antennas) in units of wavelength λ of the observed radiation $(\mathbf{r}_1 - \mathbf{r}_2)/\lambda = (u, v, 0)$. We assume that the antennas (two or more) lie in a plane, therefore only 2 coordinates are needed, u and v .

The unit vector \mathbf{s} can be written in terms of direction cosines $\mathbf{s} = (l, m)$. Here $l = \cos \phi$ and $m = \cos \theta$, where θ and ϕ are angles in spherical coordinates. Using this new notation, Equation 2.3 can be rewritten as Equation 2.4 [1].

$$V_\nu(u, v, w = 0) = \iint I_\nu(l, m) \frac{e^{-2\pi i(ul+vm)}}{\sqrt{1-l^2-m^2}} dldm \quad (2.4)$$

Usually, the antenna array is observing sources in a very small region of the sky, which allows us to further simplify Equation 2.4 (using a convenient coordinate system for the angles θ and ϕ , which correspond to the cosines l and m). You can see that in their final form, the spatial coherence and the intensity functions are related by a Fourier transform (see Equations 2.5 and 2.6) [1].

$$V_\nu(u, v) = \iint I_\nu(l, m) e^{-2\pi i(ul+vm)} dldm \quad (2.5)$$

$$I_\nu(l, m) = \iint V_\nu(u, v) e^{2\pi i(ul+vm)} dudv \quad (2.6)$$

Radio-antenna arrays have a limited number of elements, as a result the spatial coherence function $V_\nu(u, v)$ is sampled at discrete points in the (u, v) plane. Astronomers define the sampling function $S(u, v)$ to be equal to one at (u, v) points where spatial coherence was measured, and equal to zero everywhere else. The Fourier transform

of the spatial coherence function yields the dirty image $I_\nu^D(l, m)$ (Equation 2.7) [1].

$$I_\nu^D(l, m) = \iint V_\nu(u, v) S(u, v) e^{2\pi i(ul+vm)} dudv \quad (2.7)$$

The dirty beam is the convolution of the true intensity function I_ν (also known as the clean image) with the so called "point spread function", or "synthesized beam" $B(l, m)$: $I_\nu^D = I_\nu * B$ (see Equation 2.8) [1].

$$B(l, m) = \iint S(u, v) e^{2\pi i(ul+vm)} dudv \quad (2.8)$$

Consider two interferometer elements (antennas) i , and j . These receivers do not measure the visibility function $V_{i,j}$ directly, instead they measure $g_i \cdot g_j \cdot V_{i,j}$. In this context $g_i = G_i e^{i\phi_i}$ and $g_j = G_j e^{i\phi_j}$ are the complex gains of each antenna. Here G_i , G_j are antenna gain amplitudes and ϕ_i , ϕ_j are antenna gain phases.

The central idea behind radio-interferometry is to use a limited number of receivers, solve for the gain amplitudes and phases of all the antennas, and undo the convolution in order to recover the true intensity distribution I_ν [1].

2.3 Radio Antennas and Data Acquisition

So far we have assumed that interferometer elements are points that record the electromagnetic field at their location. In reality, that is not true. VLA antennas, for example, are parabolic dishes 25 meters in diameter. As a result, one has to introduce another function, $A_\nu(\mathbf{s})$, "the primary beam"¹, to account for the physical properties of the receiving element itself. As a result, Equation 2.5 will take the following form:

$$V_\nu(u, v) = \iint A_\nu(l, m) I_\nu(l, m) e^{-2\pi i(ul+vm)} dldm \quad (2.9)$$

Although it might seem that this new function complicates the matter, $A_\nu(\mathbf{s})$ actually simplifies many things because it is sharply peaked at some direction given by \mathbf{s}_0 (the tracking center of the radio-antenna) and rapidly falls off to zero in other

¹Also known as "the normalized reception pattern"

directions. The primary beam has some side lobes which are sensitive to radiation from directions other than \mathbf{s}_0 ² [1].

2.4 Coordinate Systems in Radio Interferometry

This is a short description of the coordinate system that radio astronomers use in interferometry. The baseline vector has components (u, v, w) , as shown in Figure 2.4. Here u is the coordinate in the East direction, v is the coordinate in the coordinate in the North direction, and w is the coordinate in the direction \mathbf{s}_0 . Also called "the tracking center", \mathbf{s}_0 is a unit vector pointing towards the source of interest on the sky. Any direction on the sky is specified via (l, m) , which are the direction cosines with respect to the (u, v) axes [1]. You have to be familiar with the coordinate system (especially with the way the baselines are defined) in order to reduce the data.

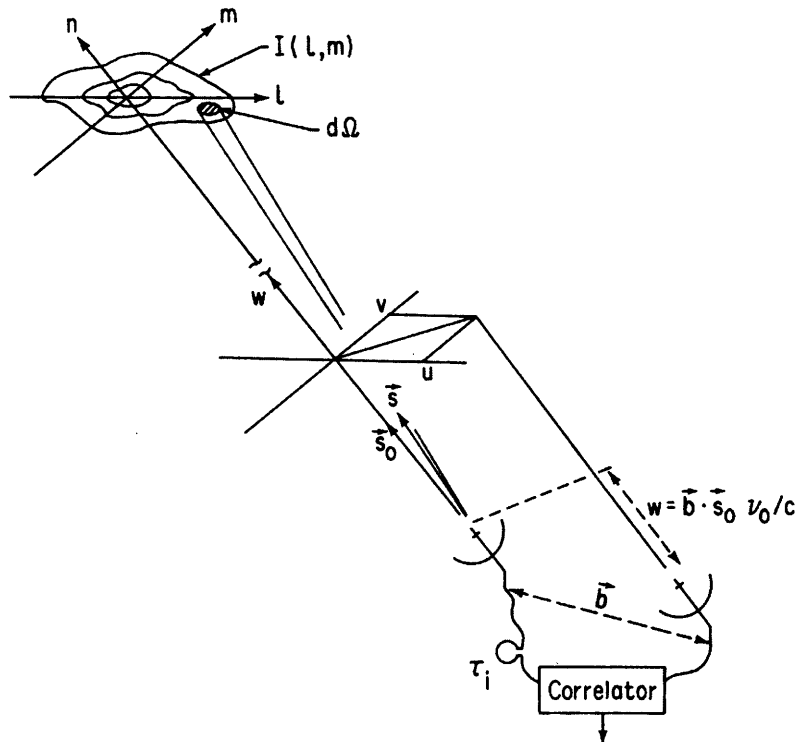


Figure 2-1: The coordinate system used for interferometer baselines. Figure scanned from page 20 of [1].

²This is also called "ground spillover".

2.5 Synthesis Array Design

The signals from each pair of antennas in an array are correlated and recorded during an observation. If there are N_A antennas, there will be $\frac{1}{2}N_A(N_A - 1)$ distinct "correlation signals" recorded. The location of each pair of antennas is described by the corresponding baseline vector (u, v, w) . One of the disadvantages of interferometers is that the electromagnetic field is sampled at distinct points in the (u, v) plane. De-convolution of the signal requires knowledge of the visibility function everywhere. Radio-astronomers can get away with a fairly uniform sampling function $S(u, v)$ and some reasonable assumptions that allow to interpolate the measured visibility at (u, v) locations not covered by the sampling function [1].

The main concern when building an interferometer is to have a uniform distribution of baseline lengths. For this project, the observations were performed using the VLA (Very Large Array). The VLA has three arms, at 120 degrees to each other. There are 9 parabolic antennas on each arm and the distance of the n^{th} antenna from the center is proportional to $n^{1.716}$ [1]. This minimizes the redundancy in (u, v) coverage. A schematic representation of the VLA is shown in Figure 2.5a. A few plots of the Sampling Function $S(u, v)$ are shown in the figure Figure 2.5b. The star-shaped sampling function is characteristic for the VLA and is the result of the antenna arrangement.

The VLA has four main configurations - A, B, C and D. The A configuration has the longest baseline lengths with the most distant telescope 21 km away from the center of the array. This configuration offers the greatest magnification and resolution. The baseline lengths decrease as the VLA is moved into the B, C, and D configurations. D is the most compact configuration, with all telescopes within 0.6 km from the center. In addition to the main configurations, there are hybrid configurations such as "BnA" or "DnC". In these cases, the antennas on the East and West arms are moved to the next configuration, whereas the antennas on the North arm are left extended to offer improved view of the sky near the galactic center.

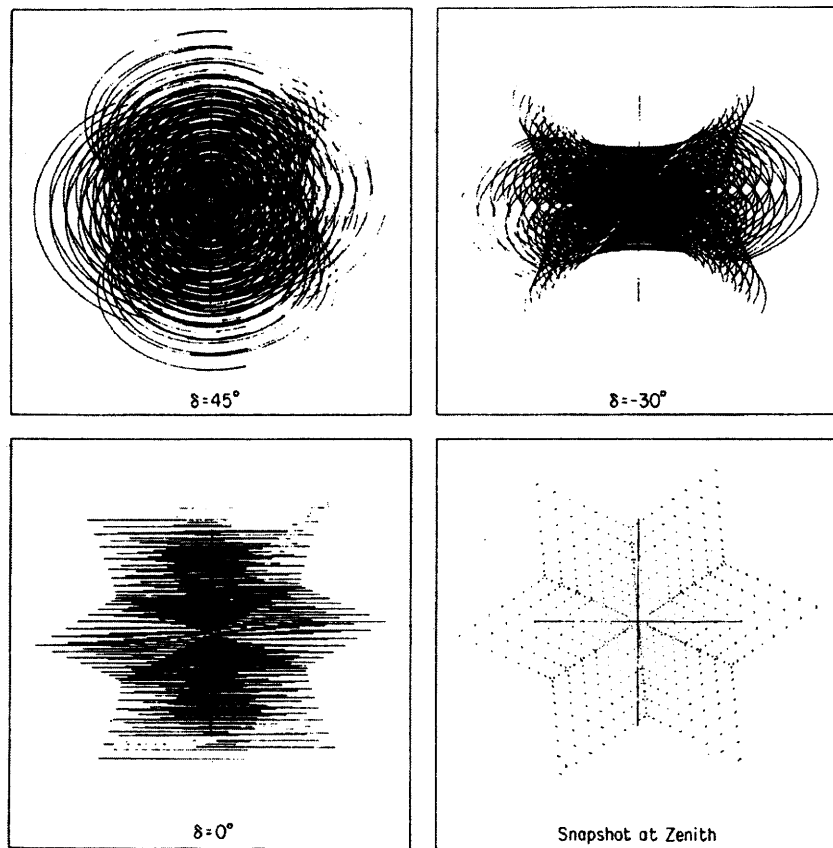
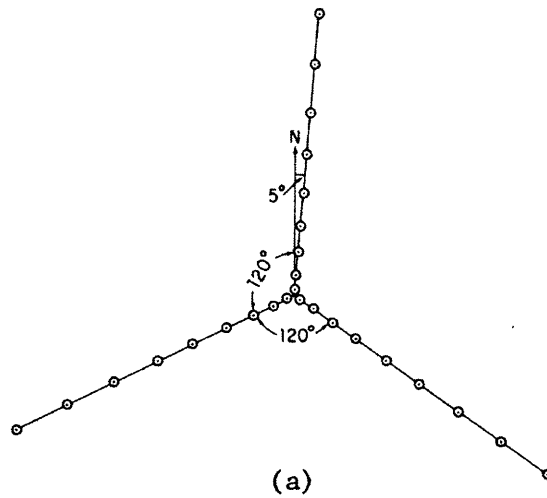


Figure 2-2: a) The configuration of the VLA with its 27 antennas. b) Examples of VLA (u, v) coverage for different declinations. The observation durations were: $\pm 4^h$ for $\delta = 0^\circ$; $\pm 4^h$ for $\delta = 45^\circ$; $\pm 3^h$ for $\delta = -30^\circ$; $\pm 5^m$ for the snapshot at Zenith. Figure scanned from page 30 of [1].

Chapter 3

Observations

3.1 Campaign Scheduling

In this campaign, observations were made with the VLA in the A, BnA, and B configurations at 8.5 GHz (VLA's X-band). These were the configurations with the longest baselines, which allowed to resolve the individual components of each gravitational lens.

The monitoring campaign had two seasons: 24 January 2002 through 18 September 2002, and 21 May 2003 through 29 January 2004. Every observation (also called epoch) lasted approximately an hour, and contained integrations on the gravitational lenses and calibrators listed in Table 3.1. There were a total of 69 epochs in Season 1, and 98 epochs in Season 2. Within a typical epoch, each gravitational lens was observed for 4-5 minutes and each calibrator was observed for 1-2 minutes. If a gravitational lens was not observable by the VLA on a particular day, additional time was allocated to the remaining sources.

3.2 Observation Layout

With a few exceptions, a primary flux calibrator was observed in every epoch. The primary flux calibrator was used as a "meter stick" to set the flux density scale for all the other sources. We chose 1734+094 as the primary flux calibrator for this

Table 3.1: The number of epochs when various sources were observed. Sometimes a particular source was not visible to the VLA at the time of observation. The top section contains the gravitational lens data, the middle section contains statistics about flux calibrators, and the bottom section of the table contains phase calibrator statistics.

Source	Season 1 [Total of 69 Epochs]	Season 2 [Total of 98 Epochs]
GL1632	65	82
GL1830	63	74
GL1838	66	78
GL2004	67	83
GL1608	54	0
1734+094	67	96
1400+621	67	80
1634+627	53	0
1545+478	67	83
2130+050	68	82
2355+498	69	78
1820-254	66	84
1651+014	65	83
2011-157	67	83
1642+689	54	0

campaign. This source has been known to be very stable over years, hence our decision to use it as the primary calibrator. The campaign also monitored secondary flux calibrators and phase calibrators (see Table 3.1).

Every observation of a gravitational lens was "sandwiched" between observations of phase calibrators. The phase calibrators associated with each gravitational lens are indicated in Table 3.2. The idea behind phase calibration is simple. Each telescope has a certain gain. The gain of the i^{th} antenna, g_i , can be expressed as a complex number, with a magnitude G_i and a phase ϕ . Phase calibrators are point-sources on the sky in the vicinity of the gravitational lens of interest. The VLA was pointed at a phase calibrator, then at the gravitational lens, then at the phase calibrator again. This was done because the phase can slowly drift while an antenna is pointing in the same direction. By pointing the telescope at the phase calibrator, then at the source

of interest and then back at the phase calibrator, one can account for the phase drift of the antenna. These phase calibrators were selected from NRAO’s Online VLA Calibrator Manual¹.

Table 3.2: Phase Calibrators Associated with Each Gravitational Lens

Gravitational Lens	Corresponding Phase Calibrator
GL1632	1651+014
GL1830	1820-254
GL1838	1820-254
GL2004	2011-157
GL1608	1642+689

In addition to phase calibrators, this campaign also monitored secondary flux calibrators. The secondary flux calibrators are Compact Symmetric Objects (CSOs). In 2001 Fassnacht and Taylor published the results of a CSO monitoring campaign and they found that CSOs have an extremely stable flux density, which makes them ideal secondary flux calibrators [23]. The campaign monitored 1400+621, 1634+627, 1545+478, 2130+050, and 2355+498 as secondary flux calibrators. CSOs are steep-spectrum radio-sources and their flux densities are expected to be constant [23].

The gain of each individual antenna might change from day to day depending on weather conditions, the state of the receiver cryogenic cooling system, and drifts in the electronics. If you observe that the flux density of a calibrator fluctuates about some average value, it means that the overall gain of the system varied slightly from epoch to epoch. If the fluctuations are correlated between secondary flux calibrators, it is an indication of instrument gain errors or flux calibration errors, rather than intrinsic source variability. One can use the secondary flux calibrators to compute the secondary gain correction for every epoch and apply this correction to other sources. This trick is occasionally used in radio-interferometry [7], [8].

¹<http://www.vla.nrao.edu/astro/calib/manual/>

Chapter 4

Data Reduction

For the initial stage of data reduction, I used NRAO's¹ AIPS² software package. The first step was to delete the bad integrations from the data, a process also known as flagging. Flagging and primary calibration was performed in AIPS. The calibrated data was then imported into DIFMAP [6] and the visibility data for every single source was visually inspected. During this stage of visual inspection, I took notes about any unflagged bad integrations leftover in a particular epoch and later re-flagged and re-calibrated that data in AIPS.

After flagging and calibration, I used DIFMAP to fit the data to source models. Each calibrator was modeled either as a point source, or a Gaussian source³. Each image of a gravitational lens was modeled as a point source or a Gaussian source. A custom PERL script was used to extract the information from Model Fit files generated by DIFMAP. MATLAB was further used for numerical analysis and light curve editing.

At the beginning, I experienced some difficulties installing both AIPS and DIFMAP in Ubuntu. I used VMware Workstation virtualization software to get around these technical difficulties. I mounted Slackware 8.0 Linux on a separate virtual machine and installed AIPS there. DIFMAP was installed on another virtual machine running

¹NRAO – National Radio Astronomy Observatory

²AIPS – Astronomical Image Processing System

³A Gaussian Source has an elliptical 2D map, it is characterized by a major axis, a minor axis and an angle that specifies the inclination of the major axis.

Fedora Core 6.0. I used PERL and Bash scripts to copy, maintain, and keep track of the numerous data files. All stages of data reduction were performed on my Pentium 4 desktop.

4.1 Initial Flagging in AIPS

Even in perfect atmospheric conditions, some of the data from an observation could be corrupt. Careful flagging of bad data was necessary to ensure high quality light-curves. I used the AIPSTV task in AIPS to display the X-band visibility data on the screen. The data was shown as a large table with rows corresponding to different integration time blocks, and columns corresponding to different VLA antennas.

At the beginning of each data inspection session, I used the QUACK task to remove data acquired in the first 10 seconds of the observation. This was done because in the initial moments of acquisition, data are noisier due to antenna settling. Some data fragments were automatically flagged at the VLA, and they appeared as blank portions in AIPSTV tables.

The default AIPSTV view was "Show Amplitude", where each pixel (data point) was given a gray-scale value (or color) proportional to the amplitude of the visibility function. Due to noise, not all the pixels had the same color. The bad integration points were identified visually since they had a different color. I used the TVFLAG task to manually flag corrupt data.

I encountered three major kinds of errors – antenna errors, temporal errors, and baseline errors. Antenna errors, as the name suggests, were associated with a specific antenna and were the most common. Sometimes the color of the entire column corresponding to faulty antenna was lighter or darker than the rest of the data. Sometimes data in the antenna column was extremely noisy (perhaps due to a higher antenna system temperature). In all these cases, data acquired by that particular antenna was flagged.

Temporal errors corresponded to periods in time when acquired data were extremely noisy or corrupted in general. In AIPSTV, temporal errors could be identified

as horizontal bands, sometimes associated with specific antennas, sometimes present in all antennas. Temporal errors were less common than antenna errors.

Baseline errors were associated with a specific baseline, for example 23-27, which means that there were errors only in the correlated signal between antennas 23 and 27. Baseline errors were rare and appeared as vertical lines in the AIPSTV data table and were easy to identify and flag.

Interferometry data were saved as FITS files. For VLA data, each FITS file contains two IF channels (i.e. two frequency bands, each is 50MHz wide) and two polarization channels – RR and LL. As a result, there are 4 layers of data that have to be flagged individually in every file: IF1RR, IF1LL, IF2RR, and IF2LL. Sometimes, errors are specific to a certain frequency channel (IF), sometimes they are specific to a polarization channel. I visually inspected each of the 4 data layers and flagged them individually.

The flagged epoch data were saved to separate FITS files with the "FG.UVF" extension (FlaGged UV-Fits file). The flagging procedure did not physically remove any data from the initial file, it created an FG (FlaG) table, where the flagged points were registered. This prevented accidental loss of data. The flag table could be deleted anytime to revert the FITS file to its original state. Note that only the flux and phase calibrators were subject to this initial round of flagging. No gravitational lens data was flagged in AIPS.

4.2 Calibration in AIPS

After the careful flagging procedure removed bad integrations from calibrator data, I used an automated AIPS script to set the flux density of the primary flux calibrator, 1734+094, in every epoch. AIPS calculated the flux densities of all the other sources by comparing them to the primary calibrator.

In the first stages of data reduction, we chose 2355+498 as the primary flux calibrator for this campaign. However, 2355+498 was observed in only 78 epochs out of 98 total epochs in the second season, an unacceptable statistics for a primary cali-

ibrator (see Table 3.1). Finally, I designated 1734+094 as the primary flux calibrator because it was observed in 67 out of 69 epochs for Season 1, and 96 out of 98 epochs for Season 2 (see Table 3.1).

4.2.1 Primary Flux Calibration

I used the AIPS task SETJY (Set Jansky) to set the flux density of the primary flux calibrator, 1734+094, to 0.48 Jy/Beam. This value was taken from the Online VLA Calibrator Manual⁴. The actual value of the flux density is not important since we are interested in the relative flux density variations of gravitational lens components. At this stage, we assumed that the primary calibrator had a constant flux density. This was motivated by the initial round of data analysis as preliminary light curves suggested that the flux of 1734+094 was constant within 0.5%. In addition, 1734+094 is on the list of recommended calibrators for the X-band in the VLA Calibrator Manual.

I used task CALIB in AIPS to perform the calibration. Using 1734+094 as a "meter stick", CALIB solved for the visibility amplitudes and phases of all the sources. The majority of the calibrators were not resolved by the VLA in A or B configurations, as a result they were treated as point-sources. However, 1400+621 and 1634+627 exhibited extended emissions from their core and were partially resolved by the interferometer.

I used the standard procedure of limiting the UV-radius for the partially resolved sources. The idea is that a partially resolved source will look like a point-source if the baseline lengths of the instrument are restricted to some maximal UV-radius. In such cases, de-convolution software uses data only from the antenna-pairs with short baselines. The UV-Radius for 1400+621 was restricted to $400k\lambda$ and the UV-Radius for 1634+627 was restricted to $200k\lambda$. NRAO recommends these values for X-band data in the VLA Calibrator Manual.

Self-Calibration in CALIB was performed in one step, with "A&P" (amplitude and phase) self calibration with a solution interval of 30 seconds. A warning was issued if

⁴It can be found at <http://www.vla.nrao.edu/astro/calib/manual/index.shtml>

phase errors were larger than 10 degrees. The calibration procedure generated a status report for each processed epoch. These reports were parsed to detect possible error messages. If the status report contained a significant number of phase calibration closure errors, or any other errors, the epoch was subject to additional flagging in AIPS. Sometimes two or more rounds of flagging were required to reduce the number of errors and warning messages.

4.2.2 AIPS File Management

After the successful completion of calibration, GETJY (Get Jansky) task in AIPS was used to extract the flux densities of the primary and secondary calibrators. I used the SPLIT task to save flagged and calibrated FITS data to separate files corresponding to individual sources in each epoch. The split FITS files and the original FITS files were saved in a separate folder for each epoch. This folder also contained the calibration status message and other files relevant to that epoch. Splitting the epoch fits files marked the end of the AIPS data reduction stage.

4.3 Data Reduction in DIFMAP

DIFMAP is a flexible radio-interferometry editing and mapping program. DIFMAP was written by Martin Shepherd [6] at Caltech and is now frequently used for VLBI and VLA data reduction.

4.3.1 Flagging Gravitational Lens Data in DIFMAP

Before any actual data analysis could be done on the GL data, bad integrations had to be flagged (recall that AIPS flagging affected only the calibrators). The split file corresponding to a source in particular epoch was loaded in DIFMAP and the visibility amplitudes and phases were plotted versus baseline UV radius.

Using DIFMAP, I visually inspected all the split fits files generated by AIPS (every source in every epoch). If a calibrator happened to contain corrupted integrations,

I took notes, loaded the original FITS file into AIPS and reflagged that particular calibrator. Then I repeated the traditional calibration, split procedures and returned to DIFMAP. This work-flow minimized the errors that could have gone otherwise undetected.

The simplest model for a gravitational lens with two images contains two point-sources. The Fourier transform of two point sources will look like a sinusoid on the UV plot. The gravitational lens data contained noise on top of the sinusoidal pattern, and this noise was especially large for faint images. Corrupted data-points were easily spotted on a UV-plot of the visibility data in DIFMAP. These points stood out as outliers and were flagged with the mouse. DIFMAP has a couple of alternative data viewing modes that can be used to flag individual points, baselines, or entire antennas.

Flagged source data were saved as FITS files that were used for source model fitting in DIFMAP (the next stage of data reduction).

4.3.2 Source Model Fitting in DIFMAP

The traditional method of interferometry data analysis is to take the radio-data and undo the convolution of the visibility function. This is usually done using the CLEAN algorithm, first introduced by Högbom in 1974 [28]. Although clean images are very useful, in our case was easier to fit models directly to the calibrated visibility data, without creating clean maps of the sources.

An automated DIFMAP script performed model fitting (see the Appendix). The source FITS file was loaded into DIFMAP and the total intensity data was selected ($I = RR+LL$). The script loaded a source model held the source positions fixed, but allowed flux densities to vary. The UV visibility data was fitted to this model. Accurate source coordinates for these models were obtained with VLBA by my thesis supervisor, Prof. J. N. Winn⁵.

A dirty map of 1024 by 1024 pixels was then created (each pixel was 0.5 arc-seconds across). First, the data underwent antenna phase self-calibration. DIFMAP then performed a series of model fitting procedures alternated by phase self-calibrations.

⁵VLBA has a much higher resolution than VLA

Model fitting continued until Chi-Squared reached a minimum. The best-fit parameters were saved to a PMOD file (PMOD – Phase Self Calibrated Model). In addition, the residual map RMS was measured and saved. The residual map RMS was later used to quantify the image noise.

After the PMOD model results were saved, the data underwent a series of amplitude self-calibration and model fitting procedures to reach a new Chi-Squared minimum. This set of best-fit parameters was saved to an AMOD file (AMOD – Amplitude self-calibrated model). The PMOD and AMOD data were processed independently in identical conditions and they were in very good agreement. In the later stages of data analysis I worked with the PMOD data because there was little difference between the two data sets.

DIFMAP model fitting scripts were ran for all the sources and epochs in this campaign. A typical source model included fixed and variable components. Only the flux density of the source was allowed to vary from epoch to epoch. This limited the degrees of freedom of the model to a minimum. The fit parameters that I used are summarized in Table 4.1.

Note that calibrators were modeled as single sources (point or Gaussian), whereas the gravitational lenses were modeled as a few individual sources, with one source per image. Unfortunately, the model for GL1830 was oversimplified. The image contains extended emission features that are partially resolved by the VLA. As a result, the apparent flux density of GL1830 components varied when the configuration of the VLA changed. To properly model this gravitational lens, we would need deep observations of the source and additional model components.

I wrote a custom PERL script to parse the AMOD, PMOD and DIFMAP log files and summarize the results in a text-file.

Table 4.1: Source Parameters used by DIFMAP model-fitting scripts. Flux Density was the only free parameter. The second column contains initial value guesses for the flux density. *Note that 1634+627 was modeled as an Elliptical Gaussian Function, whereas all the other calibrators were modeled as point sources.

Source	Flux [Jy/Beam]	Radius [mas]	Θ [Deg]
1400+621	1.0831v	0	0
1545+478	0.2994v	0	0
1634+627*	0.7971v	0	0
1642+689	1.1857v	0	0
1651+014	0.6253v	0	0
1734+094	0.5337v	0	0
1820-254	0.8796v	0	0
2011-157	1.6729v	0	0
2130+050	1.2701v	0	0
2355+498	0.8999v	0	0
GL1608 A	0.0206v	998.062	1.68796
GL1608 B	0.0106v	945.106	54.8636
GL1608 C	0.0103v	1229.51	141.577
GL1608 D	0.0035v	1128.68	-103.204
GL1632 A	0.1762v	0	0
GL1632 B	0.0146v	1468.73	122.289879
GL1830 A	5.7268v	56.6864	105.424
GL1830 B	3.8090v	946.337	-141.016
GL1838 A	0.2453v	0	0
GL1838 B	0.0175v	996.0534	-174.412
GL2004 A	0.0110v	0	0
GL2004 B	0.0110v	1126.216159	-119.3694208

Chapter 5

Light Curves

The previous step in data reduction summarized PMOD/AMOD data in a file for each individual source. This file contained a line for each epoch of observation with the following information: flux density, residual map RMS, time of observation, and source elevation during the observation.

These data were loaded into MATLAB to generate the light curves, the final goal of the data processing stage. The epoch number, hour, and minutes of the observation were used to calculate the sidereal time of the observation. The residual map RMS was used as an estimate of the intrinsic noise for each observation. The source elevation angle was used to investigate the gain elevation effects.

Time was measured in Julian Days (JD). Midnight on 24 January 2002 (JD=2,452,312) was chosen as the initial time counting moment for this campaign.

5.1 Raw Light Curves for Calibrators

Before discussing the details of light curve editing and secondary calibration, I present the raw light curves for all flux and phase calibrators (see Figures 5-1, 5-2, 5-3, 5-4, 5-5, 5-6, 5-7, 5-9, and 5-10). By “raw” light curves, I mean that they have not been edited and have not undergone secondary calibration.

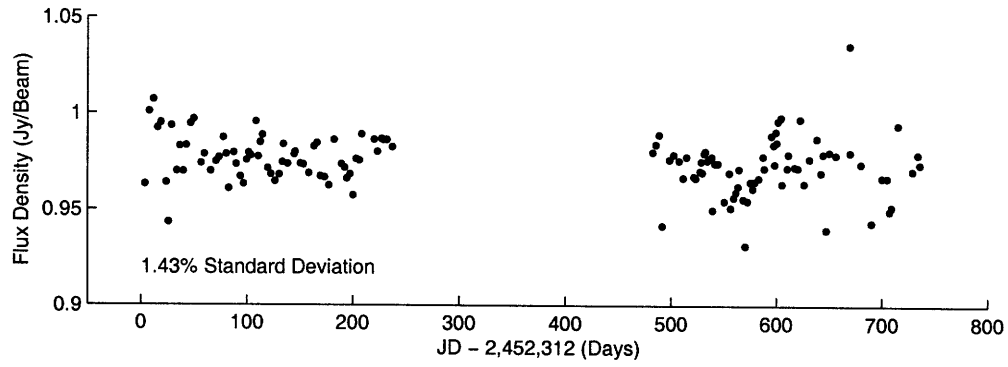


Figure 5-1: 1400+621: Initial light curve.

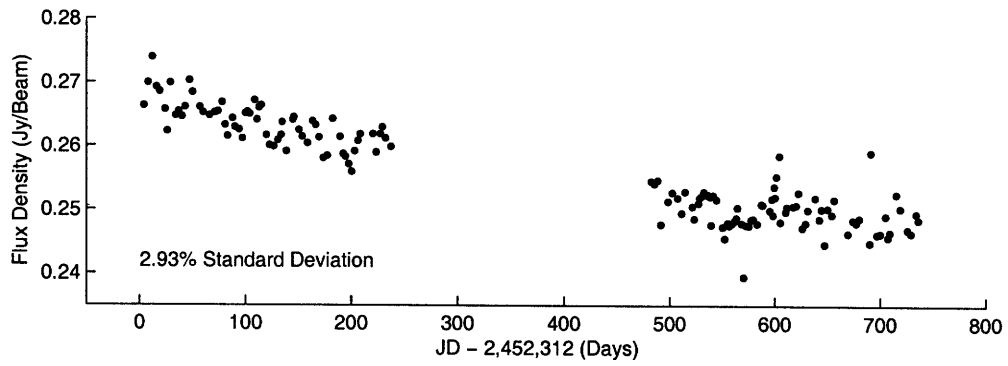


Figure 5-2: 1545+478: Initial light curve.

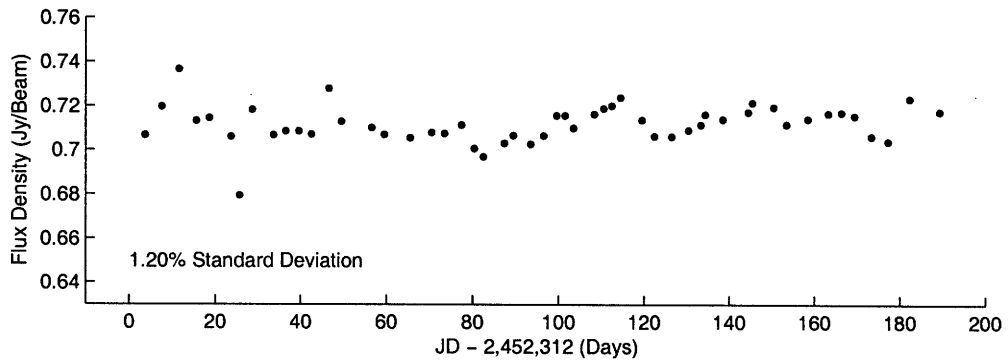


Figure 5-3: 1634+627: Initial light curve. Note that this source was observed only during Season 1.

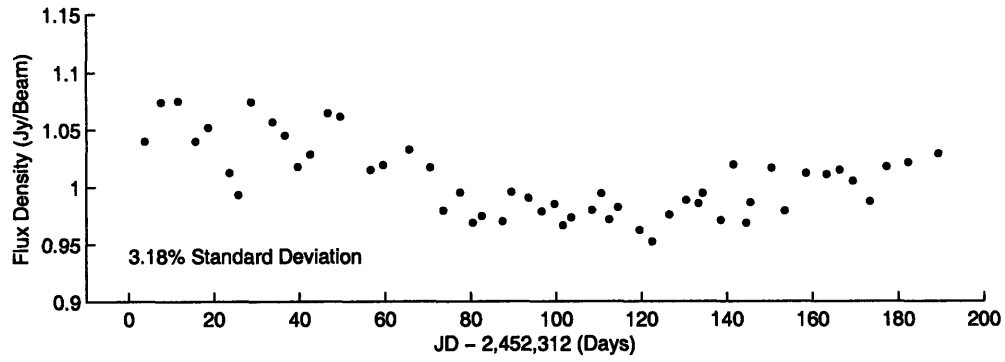


Figure 5-4: 1642+689: Initial light curve. Note that this source was observed only during Season 1.

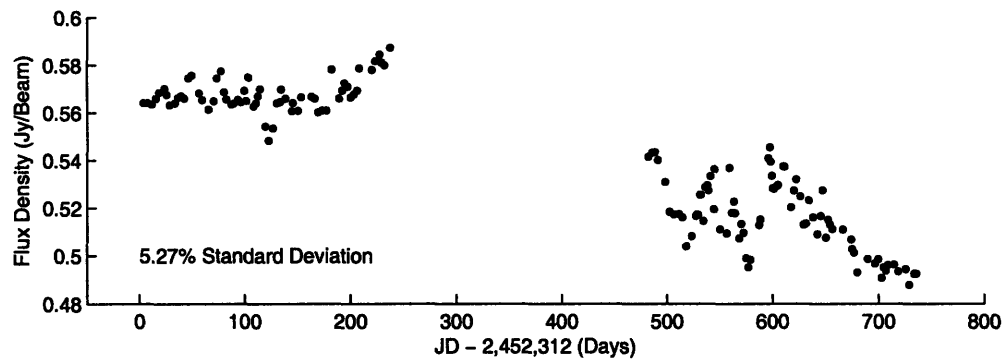


Figure 5-5: 1651+014: Initial light curve.

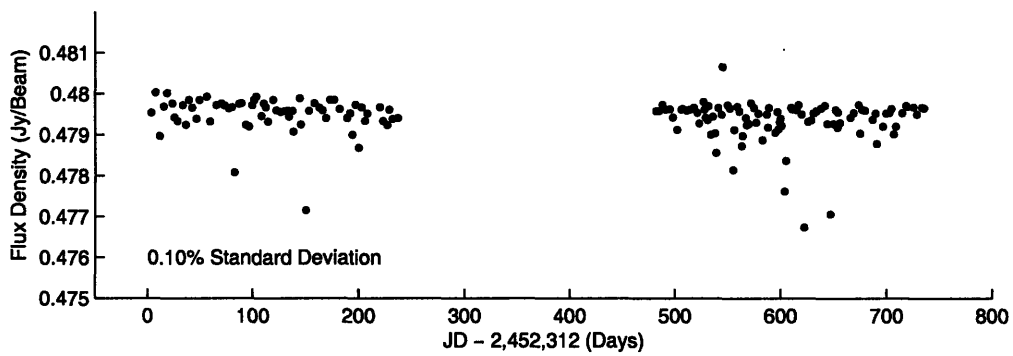


Figure 5-6: 1734+094: Initial light curve.

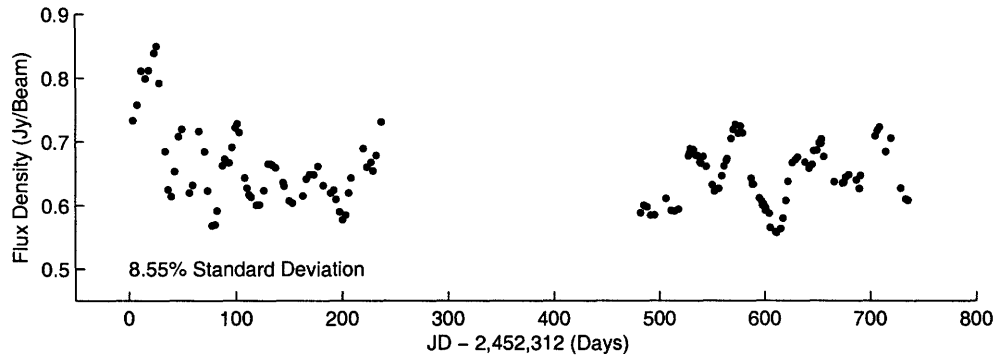


Figure 5-7: 1820-254: Initial light curve.

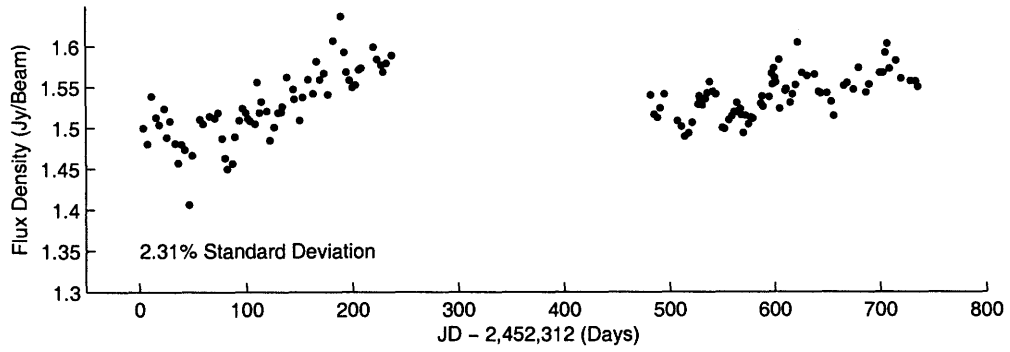


Figure 5-8: 2011-157: Initial light curve.

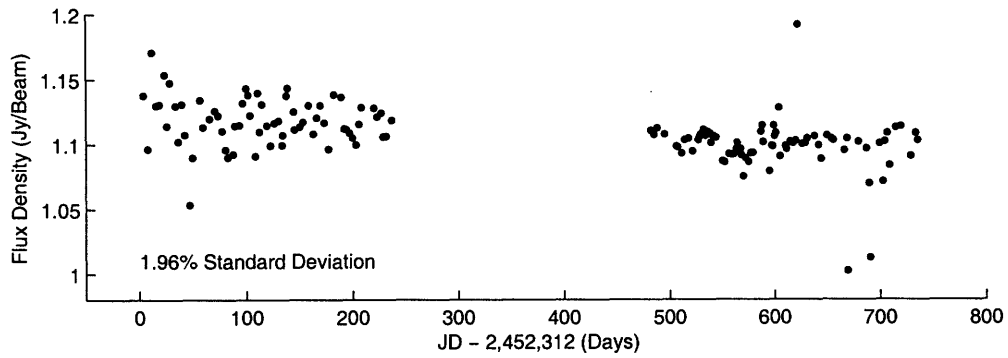


Figure 5-9: 2130+050: Initial light curve.

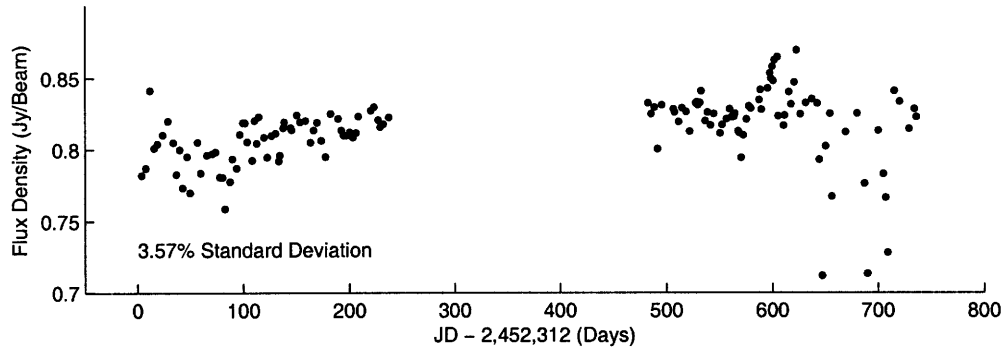


Figure 5-10: 2355+498: Initial light curve.

5.2 Light Curve Editing

I plotted the flux density versus time¹ to get the raw preliminary light curves. Even though I followed strict and careful flagging procedures, a few of the data points in my light curves were clear outliers. In order to investigate the status of outliers, I compiled a table from the OBSLOG (observation log) files provided by the VLA for each observation. This table contained the wind speed on that day, notes about hardware or software failures at the VLA data center, and notes about failures of individual antennas.

The light curve editing guidelines were simple. Any epoch missing the primary flux calibrator was automatically flagged. Following Fassnacht's example, I flagged the epochs with wind speeds in excess of 10m/sec [7]. In some epochs, significant portions of data were automatically or manually flagged. As a result, the quality of available data was poor and I flagged these epochs too.

Even after the most careful AIPS flagging, in a few cases, the AIPS calibration generated an excessive number of calibration and phase closure errors. Since I couldn't identify the problem with those epochs, I flagged them as well.

¹Time was measured in Julian Days as mentioned above

5.3 Residual Map RMS vs Expected Map RMS

The residual map RMS was measured at the end of model fitting in DIFMAP. Theoretically, the actual RMS should approach the intrinsic sensitivity of the VLA in the X-band (8.5 GHz). However, for very bright sources, such as GL1830, the VLA sensitivity is limited by the dynamic range of the instrument, which is a few thousands. The dynamic range is the ratio between the highest and the lowest visibility values that can be recorded by the instrument in the same observation. I calculated τ , the integration time on a particular source using information provided in the FITS files. The sensitivity of the VLA in the X-band is 0.049 mJy/Beam for a 10 minute long integration. The expected map RMS for an observation that lasts τ minutes is given by Equation 5.1.

$$RMS_{expected} = \sqrt{\frac{10min}{\tau}} 0.049mJy \quad (5.1)$$

I used this formula to calculate the expected RMS for each source in every epoch. The ratio of the actual map RMS to the theoretically predicted RMS varied from around 1 to 3-4 for most of the observed sources. The residual map RMS for GL1830 was a factor of 7-10 higher than the predicted RMS because of the dynamic range limitations of the VLA.

All points with an extremely high ratio of actual to predicted map RMS were verified for possible calibration errors. Such data points were investigated individually and if major errors or exceptional circumstances were detected, the point was flagged.

For the flux and phase calibrators, the actual map RMS was tiny, a fraction of a percent of the flux density. The intrinsic scatter in the light curves was comparable or larger than the residual map RMS, which suggests that there were additional sources of error, such as scintillation processes, atmospheric noise, thermal noise, and ground spill-over. I used the RMS value as a sanity check. In the latter stages of data analysis, I estimated the errors from the intrinsic scatter of the light curves.

5.4 Secondary Flux Calibration

As I mentioned earlier, this campaign monitored 5 potential secondary flux calibrators: 1400+621, 1634+627, 1545+478, 2130+050, and 2355+498. 1634+627 was only observed in the first season of the campaign, so for consistency reasons it had to be dropped from the analysis. 1400+621 was partially resolved by the VLA in A and B configurations. Even though the baseline UV radius was restricted to $400k\lambda$ during 1400+621 calibration in AIPS, the data did not look quite perfect on visibility UV-plots in DIFMAP. Taking a conservative approach, I decided to drop this source from the list of secondary flux calibrators. Finally, the light curve of 1545+478 had features that looked like real flux density fluctuations, as a result, this source was dropped too. In the end, I was left with 2130+050 and 2355+498 as the secondary flux calibrators for this campaign.

5.4.1 Gain Elevation Effect and Secondary Calibration

The gain elevation effect was mentioned in the introductory section about radio antennas. VLA antennas are large and heavy, and they deform in the gravitational field of Earth. Since gain is a function of shape, the gain is expected to vary slightly as a function of antenna elevation. Other phenomena such as thermal expansion and ground spill-over² are also likely to affect the gain of a parabolic antenna.

The usual way to account for gain-elevation effects is to apply corrections to the data during the AIPS calibration procedure. Although Prof. Winn provided a set of gain elevation correction parameters, we were not confident about the accuracy of those parameters and decided not to use them. We chose to correct for the gain elevation effect via secondary flux calibration.

To find out if our data were affected by any gain-elevation effects, I plotted the flux density of secondary flux calibrators³ versus antenna elevation angle for the first and second seasons separately (see Figure 5-11). Curiously enough, the first season

²When an antenna is sensitive to radiation emitted by the ground

³From now on I will refer to 2130+050 and 2355+498 as the Secondary Flux Calibrators

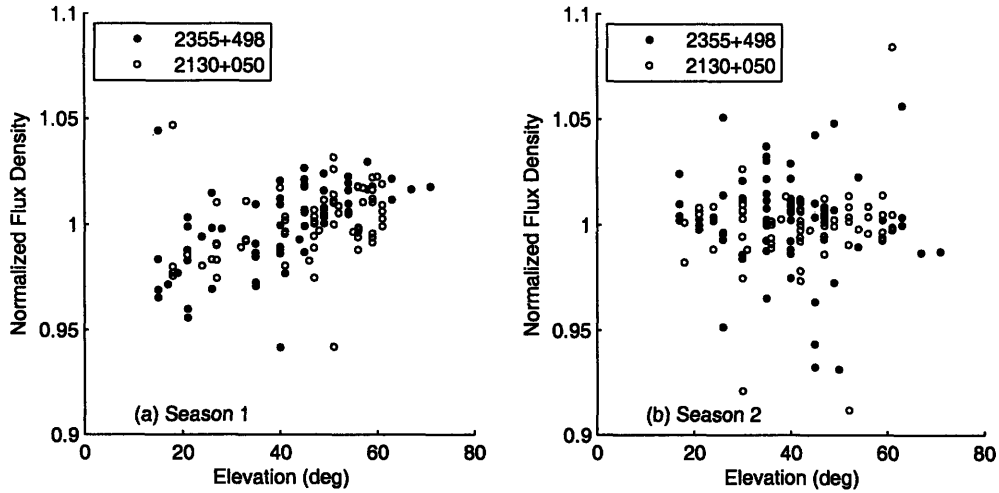


Figure 5-11: Gain Elevation Effects for Season 1 and Season 2 respectively.

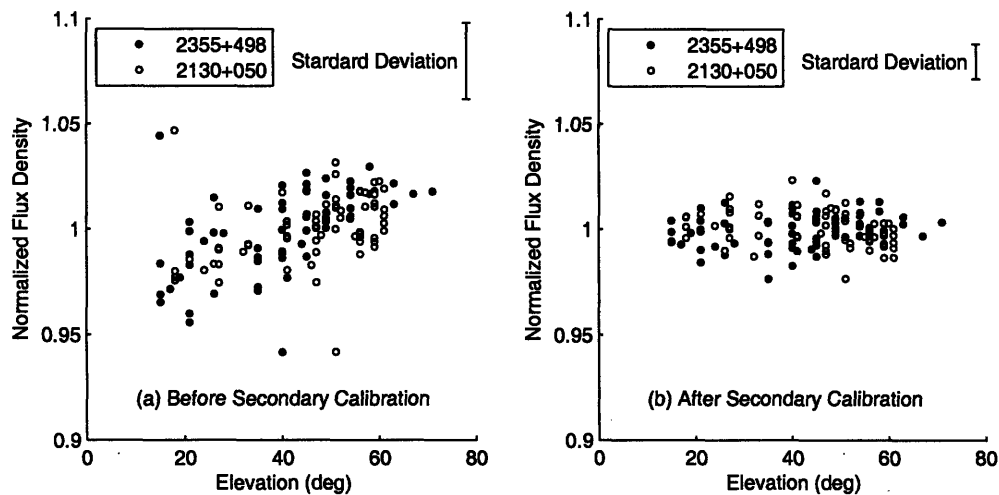


Figure 5-12: Gain Elevation Effect Correction for Season 1. Note how the secondary flux calibration cancels out the gain elevation effect and reduces the scatter in the light curves.

data exhibits a clear gain-elevation effect, whereas the second season data does not. It turns out that the VLA data center started to automatically apply elevation correction to all VLA observations sometime between the first and the second season.

I had a few options to correct the gain elevation effect for Season 1. The simplest approach was to calculate the gain elevation correction parameters by fitting a line to the plot of calibrator flux density vs elevation. This way I would be able to calculate

the expected gain-elevation effect for a given elevation and therefore correct for this effect. The second approach goes more along the lines of secondary gain calibration as defined by Fassnacht in his 1999 paper about the GL1608 delay measurements [7]. The third approach would have been to start over from scratch and use the gain elevation correction parameters supplied by NRAO to re-calibrate Season 1 data in AIPS. However, we considered this option not worthwhile, especially since it is a very time consuming operation.

Fassnacht's idea is simple – proper secondary calibration is based on the assumption that the overall VLA system gain might change very slightly from day to day. Since secondary gain calibrators are assumed to be intrinsically constant, any fluctuations in the light curves of the secondary calibrators must be because of day-to-day gain variations. The self-normalized light curves of the secondary calibrations can be summed and averaged to obtain the "secondary gain" curve, which assigns a gain correction to each epoch. When applied to the light curves of all monitored sources (except the primary flux calibrator⁴), this gain correction curve is supposed to reduce the scatter and improve the quality of the data.

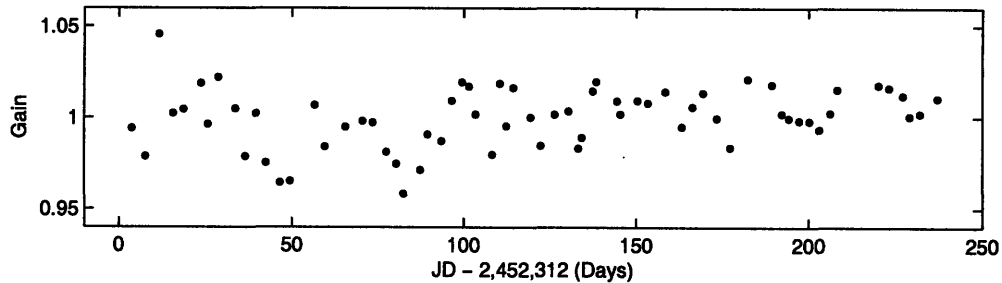


Figure 5-13: Secondary Calibration Gain plot for Season 1 Data

When I applied the secondary gain curve correction to the first season data, not only did it reduce the scatter in the light curves of all the sources, but it also canceled out the gain-elevation effect (see Figure 5-12). This makes sense when you take into account the fact that secondary calibrators were located at about the same elevation

⁴The Primary Flux Calibrator was used to set the flux density scale and required no gain elevation correction.

as the other monitored sources⁵.

When I applied the secondary calibration gain curve to data from Season 2, it failed to reduce the scatter in the light curves. On the contrary, in some light curve it increased the scatter a bit. This way, I convinced myself that the purpose of the secondary calibration was to remove the gain-elevation effect. I applied the secondary gain calibration based on 2130+050 and 2355+498 data only to Season 1. No secondary calibration was applied to the data in Season 2.

⁵This is especially true for phase calibrators, because they have to be as close as possible to a gravitational lens in order to minimize the amount of telescope movement for the "sandwich" observations Phase Calibrator - Gravitational Lens - Phase Calibrator.

Chapter 6

Time Delay Measurements

6.1 Final Light Curves for Gravitational Lenses

Before discussing the actual time delay measurement procedures, I present the final light curves (see Figures 6-1, 6-2, 6-3, 6-4, and 6-5). By saying “final” light curves, I mean that these light curves have undergone secondary calibration and are ready to be analyzed with the Pelt dispersion method.

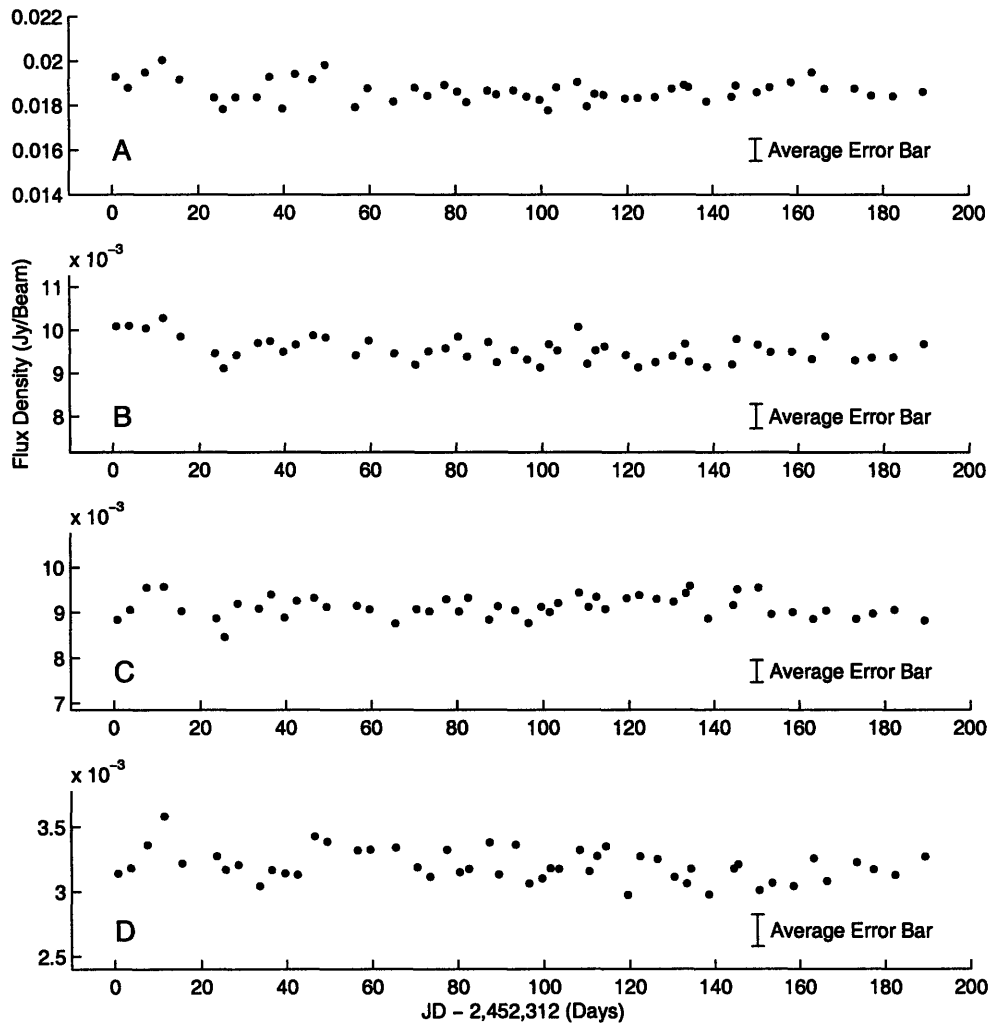


Figure 6-1: GL1608: Final light curves. Fractional flux variations are the same for all subplots. Residual map RMS is comparable to the symbol size on the plot.

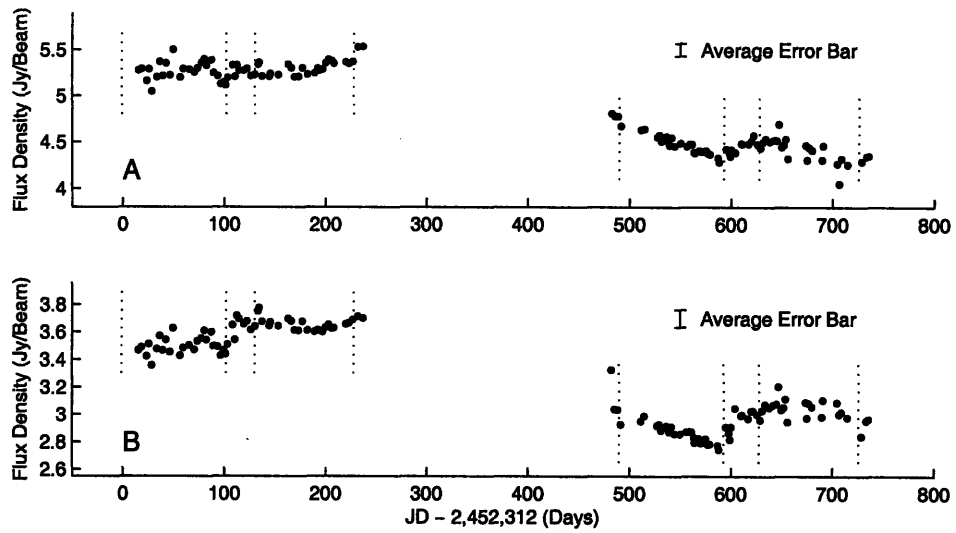


Figure 6-2: GL1830: Final light curves. Fractional flux variations are the same in both subplots. Residual map RMS is smaller than the symbol size on the plot. Note that the dotted vertical lines denote the VLA configuration changes. In order, from left to right: D→A, A→BnA, BnA→B, B→C, [break], D→A, A→BnA, BnA→B, B→C.

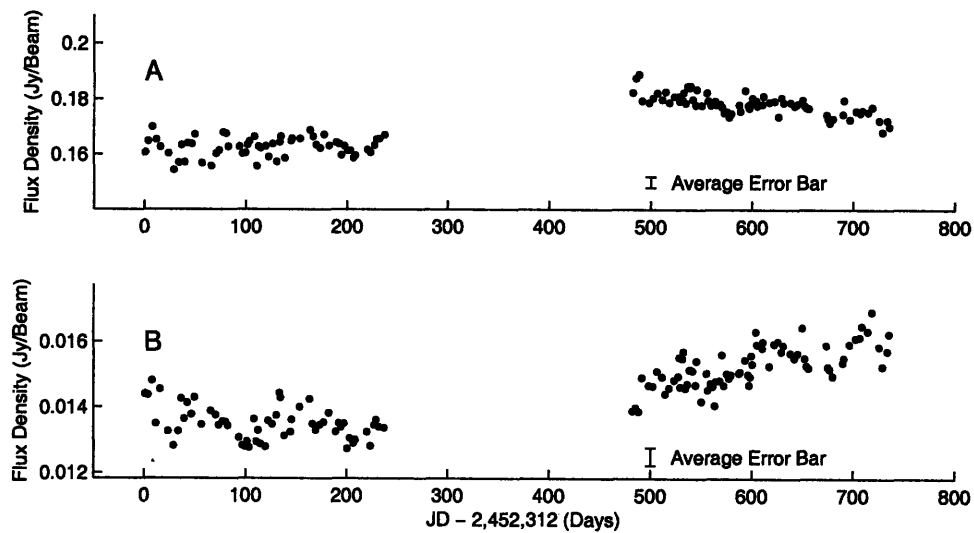


Figure 6-3: GL1632: Final light curves. Fractional flux variations are the same for images A and B. Residual map RMS is smaller than the symbol size on the plot.

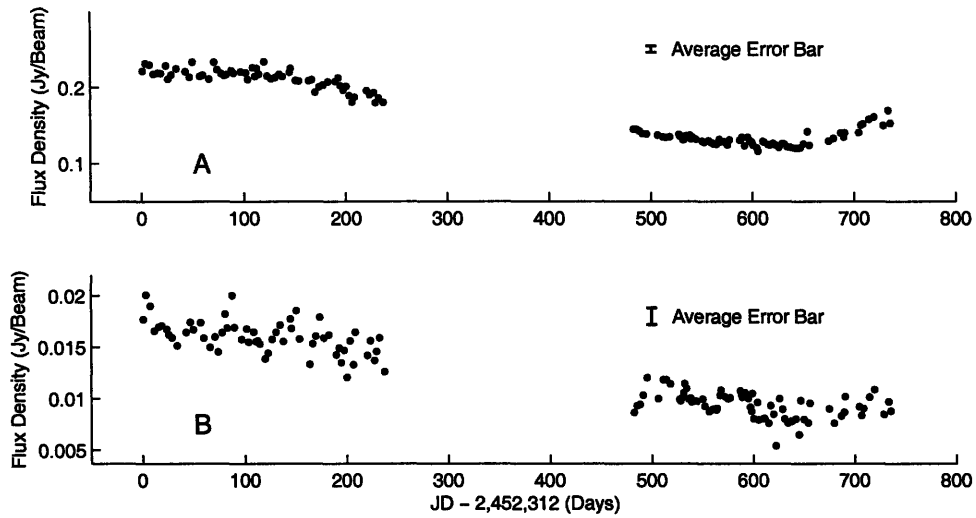


Figure 6-4: GL1838: Final light curves. Fractional flux variations are the same for images A and B. Note that the light curve of Image B is considerably noisier than that of Image A.

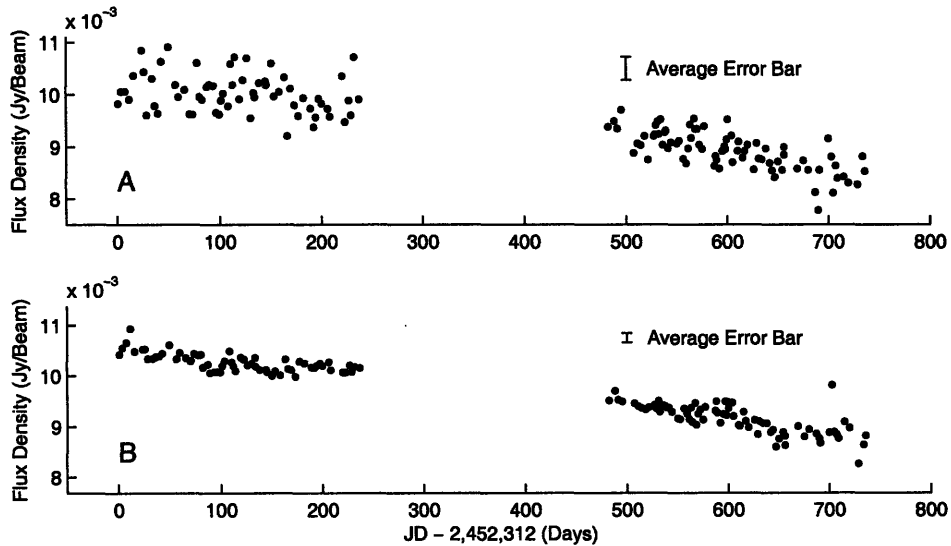


Figure 6-5: GL2004: Final light curves. Fractional flux variations are the same on both plots. Note that Image A is considerable noisier than Image B.

6.2 Measuring The Time Delays

There are several mathematical methods one can use to measure the time delay between two different images of a gravitational lens. Most of these methods involve

calculating some parameter that quantifies the correlation of the light curves and then minimizing (or maximizing) this parameter as a function of trial time delays and the flux ratio between images.

One of the most reliable and robust algorithms for time delay measurement is the dispersion method formulated by Pelt et al. in 1994 [33]. This method was first used to investigate a controversial time delay measurement for QSO 0957+561 [33]. As more and more lens monitoring data became available, Pelt's method became one of the standard ways to compute time delays [7], [8], [26]. I used this method to analyze the final light curves of GL1838, GL2004, and GL1632.

The light curves for GL1608 are fairly flat and contain no recognizable features. One can tell simply by visual inspection that any sort of statistical processing would not give a meaningful result. Note that J. N. Winn stopped monitoring GL1608 two thirds into Season 1 of this campaign, as a result we do not possess enough data to calculate the time delays. Moreover, all three time delays have already been accurately measured by Fassnacht et al. [8]. Based on these reasons, I decided to drop GL1608 from this analysis.

The light curves for GL1830 show flux variations at the transitions between different VLA configurations (i.e. when the antennas are moved to change the baseline lengths). This is because our DIFMAP source model for GL1830 was oversimplified. It assumed that the lens image contained two compact components. The original paper announcing the discovery of GL1830 mentioned that the image contained extended emissions and a partial Einstein ring, which require more sophisticated modeling [14]. I did not have enough time to re-model this gravitational lens, but I will repeat the DIFMAP fitting procedure after this thesis is completed.

6.3 Error Estimation

In the previous chapter, I mentioned that the point scatter in the light curves of monitored gravitational lenses was either comparable to, or significantly larger than the residual map RMS. This scatter is a result of various noise-generating processes

such as scintillation, ground spill-over, thermal noise in the antennas, and perhaps micro-lensing. Some of the scatter could be attributed to undetected calibration errors. Anything other than intrinsic source variation will be treated as noise.

To properly analyze the data, I needed a realistic estimate of the error bars. The flux density of a gravitational lens image should not vary significantly on time-scales of days [7]. Therefore any short term variation in the light curves of GL images is noise. I used N-point median smoothing filtering to smooth the light curves. The filter takes the median value for every N neighboring points. The number N has to be odd. One of the advantages of this filter is that it is immune to outliers¹.

Given the input curve X_i , the smoothed curve X_j^{smooth} is the median of $X_{j-\frac{N-1}{2}}, \dots, X_{j+\frac{N-1}{2}}$. It is tricky to define the median filter at the beginning and end of the data set. In these cases, I computed the smoothed curve using the nearest N points, which caused the filter output to flatten at the beginning and end of the light curves.

The length of the filter has to be long enough to ensure smoothing, but short enough to avoid smoothing over real variations in the light curve (especially at the beginning and end of a season). Since we do not know the characteristic timescale of GL variations, we have to choose the smoothing filter length based on common sense and the properties of the light curves.

$$\varepsilon_i = X_i - X_i^{smooth} \quad (6.1)$$

I defined the scatter error ε as the difference between the real and smoothed light curves (see Equation 6.1). These error estimates were used to generate simulated light curves in the final stage of analysis.

6.4 Pelt's Dispersion Method

One of the main advantages of this method is that it does not require re-sampling the data, it works with randomly sampled data sets. Other time delay calculation methods require interpolating the light-curves, which can introduce additional errors

¹Note that outliers do affect averaging filters

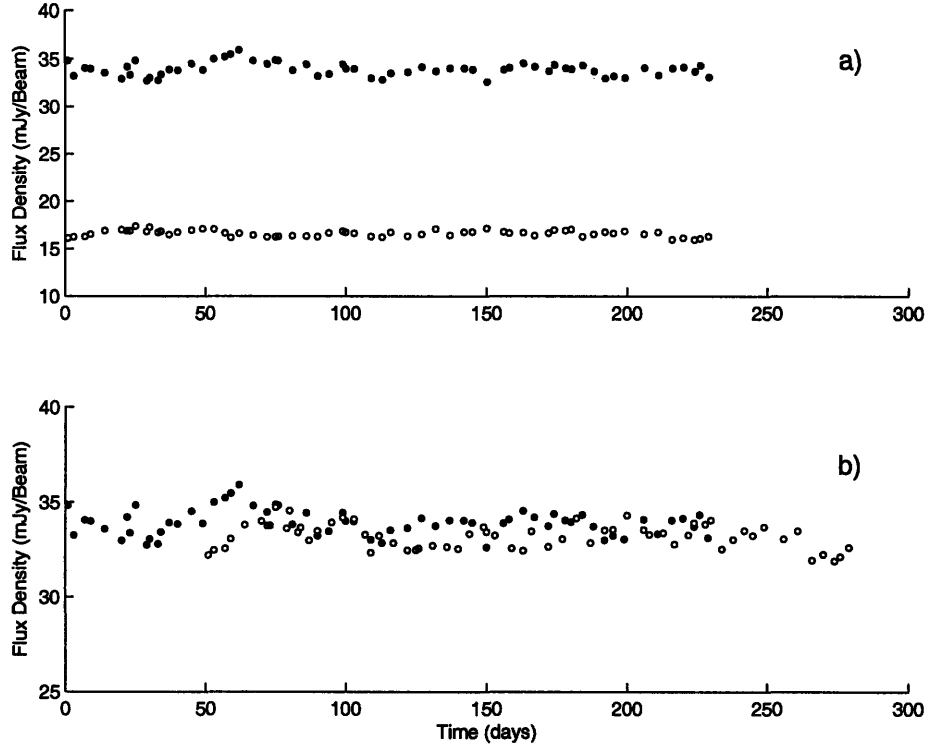


Figure 6-6: Creating a combined light curve (b) using raw light curves from (a). The first curve (solid circles) was left unchanged, while the second curve (empty circles) was magnified by a factor of $M=2$ and shifted forward in time by 50 days.

and make the results depend on the interpolation method. For a gravitational lens with two components, A and B, the flux densities $A(t)$ and $B(t)$ can be expressed as written in Equation 6.2 [31].

$$A(t) = C_A + a(t) + \Delta A(t) \quad (6.2)$$

$$B(t) = C_B + M \cdot a(t - \tau_{AB}) + \Delta B(t) \quad (6.3)$$

Here C_A and C_B are constant flux components; $a(t)$ and $M \cdot a(t - \tau_{AB})$ are the variable components; $\Delta A(t)$ and $\Delta B(t)$ represent the noise. I assumed that image B lags behind image A with a time-delay τ_{AB} ² and the magnification ratio is M . It is natural to assume that images formed by a gravitational lens might contain constant

²If A lags behind B, the calculated time delay will be negative ($\tau_{AB} = -\tau_{BA}$).

flux density components C_A and C_B . For example, if the background source is a galaxy with an active black hole in the center, the central region of the galaxy would have a variable flux density, whereas the outskirts of the galaxy and any extended jets would have a constant flux density.

The magnification ratio, M , might change slowly over long periods of time because of microlensing. When data is acquired during multiple seasons, it is a common practice to allow the magnification ratio to vary independently from season to season [8], [31]. Significant variations of the magnification ratio from season to season are not expected, unless there were micro-lensing effects involved.

Pelt's method requires you to create a combined light curve from the individual light curves of two distinct images. Then the dispersion of the combined curve is computed using Formula 6.5. The dispersion is a number that quantifies the scatter of the combined light curve. The more scattered the points, the larger the dispersion. In Pelt's method, one of the original light curves, for example $A(t)$, is left intact. The other light curve, $B(t)$, is scaled in magnitude, shifted in time, and then combined with $A(t)$, as shown in Figure 6-6. Consider the formulas in Equation 6.2. The shifted and scaled light-curve for image B would be calculated using Equation 6.4.

$$B'(t) = \frac{1}{M} [B(t + \Delta T) - C_B + C_A] \quad (6.4)$$

The trial time delay, ΔT , is a variable parameter. Ideally, in the absence of noise, when the trial delay equals the real time delay, $\Delta T = \tau_{AB}$, the light curves $A(t)$ and $B'(t)$ should be identical. The constant flux components C_A and C_B are degenerate, so they can be replaced by a single parameter $C = C_A - C_B$ ³.

The idea behind Pelt's method is to vary the trial time-delay, calculate a scaled and time-shifted curve $B'(t)$, and then superimpose it with $A(t)$. This way, the combined light curve $S(t)$ is obtained. For every trial time delay, the dispersion of the combined curve is computed. The dispersion minimum corresponds to the time-delay between signals $A(t)$ and $B(t)$. Obviously, this analysis cannot provide meaningful results if

³We are interested in the variable components of each image. In this context we are not interested in the actual value of the constant components.

the signals are too noisy, or if the signals do not contain real variations.

The simplest way to calculate the Pelt dispersion is to look at every data point in the combined light curve and compute its dispersion contribution. The expression for D_1^2 Pelt dispersion is given in Equation 6.5 [33].

$$D_1^2 = \frac{\sum_{i,j} W_{i,j} G_{i,j} T_{i,j} (S(t_i) - S(t_j))^2}{2 \sum_{i,j} W_{i,j} G_{i,j} T_{i,j}} \quad (6.5)$$

Here $G(i, j)$ is the neighbor selection factor. $G(i, j) = 1$ if the points i and j come from two different light curves $A(t)$ and $B(t)$. $G(i, j) = 0$ otherwise. This way, Pelt dispersion accounts only for correlation of points from different light-curves. This method ignores the contributions due to intrinsic scatter of individual light-curves (intrinsic scatter is accounted for during error estimation).

$W_{i,j}$ is the pair weighting factor. One could use uniform weighting, in which case the contribution of any pair of points (i, j) is weighed with $W_{i,j} = 1$. Another common weighting scheme is quadratic weighting: $W_{i,j} = 1/\delta_i^2 + 1/\delta_j^2$, where δ_i and δ_j are the uncertainties for points i and j .

$T_{i,j}$ is the time de-correlation selection factor. We assume that distant points on the light-curve are not correlated. If the temporal separation between points i and j is less than the de-correlation time T_{decorr} , then $T_{i,j} = 1$, otherwise $T_{i,j} = 0$. The de-correlation timescale is a parameter that has to be adjusted. I used $T_{decorr} = 10$ days for all my calculations.

6.5 Searching the Parameter Space

In order to perform dispersion analysis and calculate the time delay, I had to calculate the magnification ratio M and the constant flux component C . For each lens, I created a trial time delay vector T_i , a trial magnification vector M_j , and a trial constant component vector C_k . MATLAB scripts generated the combined light curves for all possible combinations of M_i , C_j , and T_k and calculated the dispersion $D_{i,j,k} = D(M_i, C_j, T_k)$.

In order to search the parameter space (M_i, C_j) , I minimized the dispersion function. I assumed that the lowest dispersion value corresponded to the best-fit M_i and C_j values. The magnification ratio was initially estimated roughly by dividing the average flux densities of two images. The constant flux parameter was allowed to vary in the interval $-\langle B \rangle \leq C \leq \langle A \rangle$, where $\langle A \rangle$ and $\langle B \rangle$ are the average flux densities of the two GL images.

I searched the parameter space with a brute force approach, i.e. calculated the dispersion for a 3D grid of M_i , C_j , and T_k values⁴ and found the minimum value of D_1^2 on this grid. The M_i and C_j grid spacing was initially rough, but I performed iterative calculations, each time decreasing the parameter search space and refining the grid. In the initial stage of calculations, I discovered that the best fit for the constant flux component C , was sometimes quite large, especially for GL2004 and GL1838.

If the lens is subject to differential scintillation (i.e. one component scintillates more than the other), the parameter searching procedure finds large values for C because the relative scatter of each light curve is different. Winn et. al experienced this same numerical problem when they analyzed ATCA⁵ data in an attempt to measure the GL1838 time delay[16].

All this time I have been using the concept that a gravitational lens image is supposed to have a constant and a variable component. The idea behind it is simple – the background galaxy (which is being imaged by the lens) may have compact components and extended components. A compact component is small enough such that the light-travel time across it is small. The compact components are known to vary coherently. Extended components (jets and Einstein rings) are large scale structures and it takes light a significant amount of time to cross them. As a result, any variations are averaged out and extended components remain approximately constant.

Since GL1632, GL1838, and GL2004 all consist of compact components, I decided to drop the constant flux component from the calculations and assumed that $C = 0$

⁴This method was simple and reliable, but computationally intensive.

⁵Australia Telescope Compact Array

for all three lenses. C must be taken into account when the lens images contain extended jets and structure such as Einstein Rings. Among the 5 lenses monitored in this campaign, only GL1830 would require the inclusion of a constant flux component.

With C out of the picture, the parameter search space became much smaller and this simplification was advantageous from a computational point of view. I allowed the magnification ratio M to vary independently in Season 1 and Season 2. Any variations in M from season to season can be attributed either to micro-lensing or to the the fact that the lens has a time delay comparable to the length of the campaign.

6.6 Simulations

If the light curves of gravitational lens images contain significant variability, it should be possible to calculate the time delay by matching prominent features in different light curves. It is usually a combination of luck and persistent monitoring that allow astronomers to calculate the time delay. The dispersion curve $D_1^2 = D_1^2(T_i)$ ⁶ will always have a minimum. How do you find out whether this minimum corresponds to the actual time delay or is simply a statistical accident?

The common practice is to use Monte Carlo simulations to test the statistical reliability of tentative time delay measurements. The main idea is to create simulated light curves $A_{sim}(t)$ and $B_{sim}(t)$ from the original light curves $A(t)$ and $B(t)$ and repeat the Pelt analysis several times using simulated light curves. The goal is to keep data characteristics and noise spectrum the same. Pelt et al. [33], and Fassnacht et al. [7] suggested using the smoothed light curves $A_{smooth}(t)$, and $B_{smooth}(t)$ as "generating light curves". The original error-bars, $\epsilon_A(t)$, $\epsilon_B(t)$, are shuffled and put back onto the "generating light curve" to produce simulated curves. As a result, the simulated light curves will carry the same information (i.e. intrinsic flux density variation) and will have the same noise properties as the original curves. The Pelt dispersion calculation is repeated for the simulated curves using the previously calculated lens magnification M ⁷.

⁶Here T_i is the trial time delay

⁷One could in fact re-calculate the magnification ratio for each light curve, but it turns out to be

Different simulated light curves are expected to have dispersion minima corresponding to different time delays. If the time delay histogram for a large number of simulations has a clearly defined maximum, this means that the measured time delay is statistically reliable. The histogram can ultimately be used to estimate the mean time delay and the σ and 2σ confidence levels. I performed 10000 simulations for each gravitational lens.

6.6.1 Code Testing on GL1608 Data from Fassnacht et al.

I wrote the data-crunching code in MATLAB. Prior to using the code on my own light curves, I tested and debugged it using GL1608 Season 1 data from Fassnacht's monitoring campaign [7] (see Figure 6-7). Fassnacht et al. managed to calculate all three time delays for this four-image system. For simplicity, I worked with the brightest components, A and B. In the first paper announcing the measurement of the GL1608 time delay, Fassnacht et al. calculated that image A lagged behind image B with time delay $T_{BA} = 31^{+3}_{-2}$ days (68% confidence interval) [7].

The accuracy of this measurement was later improved using data from two additional monitoring seasons [8]. Note that Season 2 data alone could not be used for a time-delay measurement because it did not have any distinct features that could be related to each other.

I calculated a magnification ratio $S_A : S_B = 2.039$ which is in good agreement with the value of 2.042 calculated by Fassnacht et al. [7]. I used a 5-point median filter to smooth the original light curves and estimate the errors ⁸ (see Figure 6-8). 10000 Monte Carlo simulations generated the histogram in Figure 6-9. I managed to reproduce the result from [7], which suggests that my code was robust. The uncertainty estimate for my result, $\tau_{BA} = 30^{+4}_{-7.5}$ days (68% confidence interval), is somewhat conservative. I conclude that the Monte-Carlo simulation technique tends to overestimate measurement uncertainties.

very close to the original M , and requires a significant amount of additional computation.

⁸A longer filter caused the smooth light curve to flatten out at the beginning of the season, and thus miss some variation in component B.

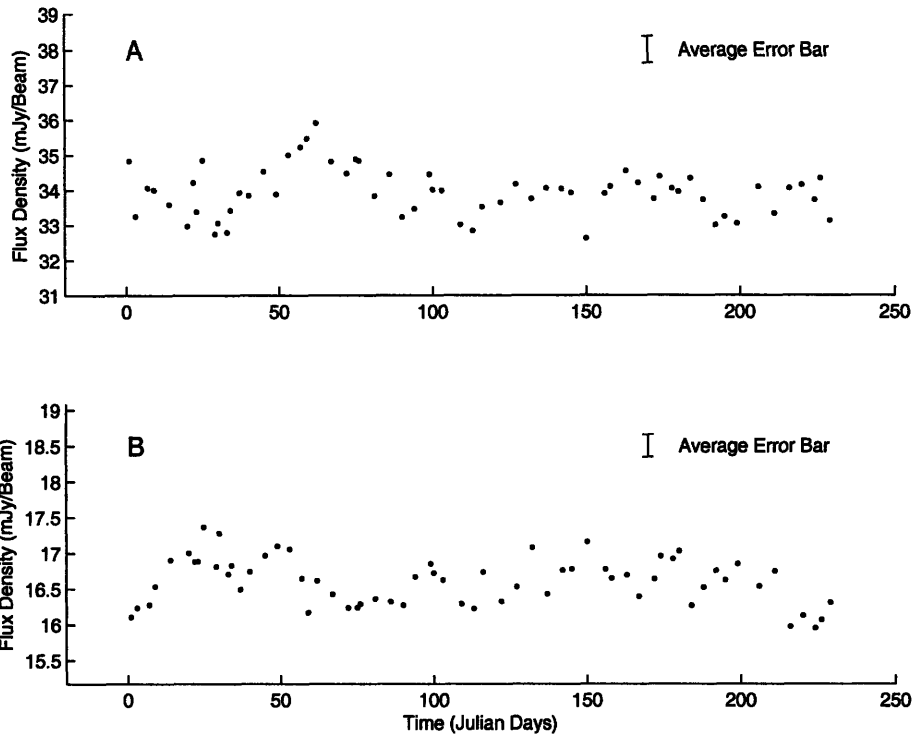


Figure 6-7: GL1608: Season 1 Light Curves of Images A and B from Fassnacht et al. [7]. The fractional flux variations are the same on both plots.

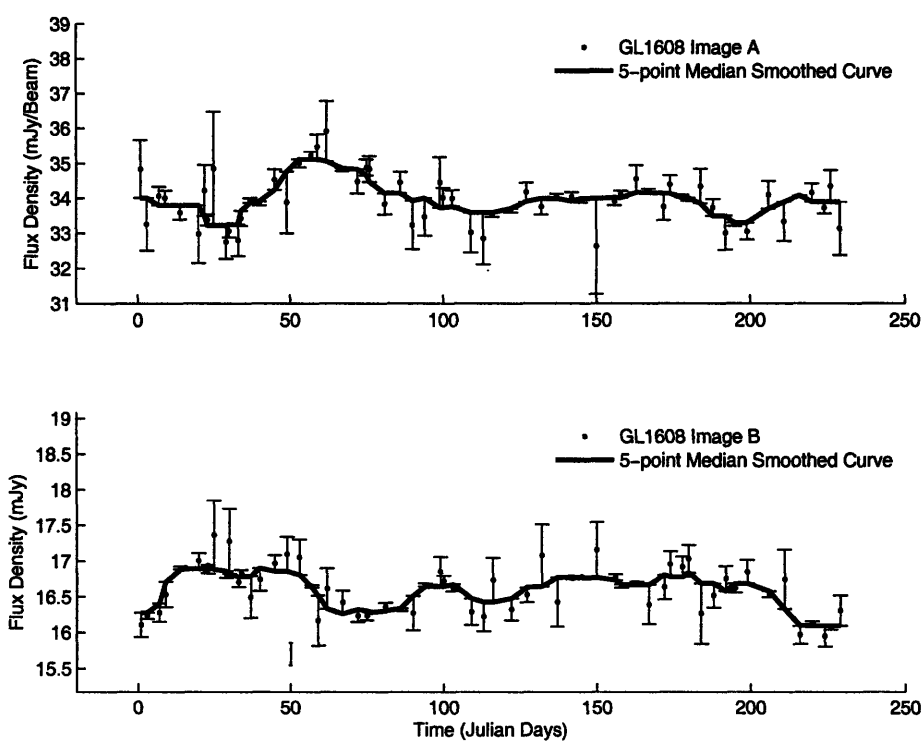


Figure 6-8: GL1608: Season 1 Smoothed Light Curves of Images A and B. Fractional flux variations are the same on both plots.

6.7 Simulation Results

6.7.1 GL1632

The final light curves and the smoothed light curves for GL1632 are presented in Figures 6-3 and 6-12. The best fit magnification ratios for GL1632 are $M_1 = 12.156$ and $M_2 = 11.340$ for Seasons 1 and 2 respectively. The dispersion plot for the original data, shown in Figure 6-14, has a minimum at 182 days. The results of 10000 Monte Carlo simulations (see Figure 6-13) show a broad peak in the region between 150 and 200 days. The histogram suggests a time delay $\tau_{AB} = 156^{+38}_{-70}$ days (68% confidence interval).

This is a very conservative estimate. When analyzing Fassnacht's data, we have seen that the histogram-based uncertainty calculation procedure tends to overestimate the errors. A much simpler way to estimate the uncertainty is to look at the dispersion plot in Figure 6-14 and identify the boundaries of the dip corresponding to the minimum. The cusp corresponding to the minimum in the $D_1^2(\tau)$ function flattens out at $\tau_{left} \approx 152$ days. I will consider this the lower boundary of the time delay measurement. On the right, the peak in Pelt dispersion at $\tau_{right} = 190$ days defines the upper boundary of this time delay measurement. I estimated the measurement uncertainties based solely on the dispersion plot from Figure 6-14, and obtained $\tau_{AB} = 182^{+8}_{-30}$ days.

This result cannot be taken without a grain of salt. We have not monitored the lens for periods significantly longer than its time delay. Unfortunately, VLA campaigns can not be continuous because the interferometer configuration changes every ~ 4 months.

In this context, I would like to introduce the concept of data window function, used by Pelt et al. [33], and Cohen et al. [26]. The window function value equals the number of pairs of data points that contribute to the dispersion calculation for a trial time delay. If the trial time delay is small, the light curves of A and B components are shifted very little in time and they maintain a significant overlap. As a result, the data window function is large for small time delays. If the trial time delay is

very large, the amount of overlap between the light curves decreases significantly and eventually reaches zero, as shown in Figure 6-16 for GL1632.

I would like to point out that the value of the window function for GL1632 data becomes very small for time delays of 150-200 days. This makes the dispersion analysis more susceptible to noise. A very low value of the window function above 200 days explains the last spike in the histogram from Figure 6-13.

The GL1632 time delay predicted from simple lens models is approximately $h\Delta\tau \approx 120 - 130$ days [15]. The exact value depends on the model of the lensing galaxy. The tentative time delay suggested by my analysis is of the same order of magnitude. However, for such a long time delay, the gravitational lens must be monitored continuously for a few years to maintain a reasonable data window. On the bright side, our data indicates that GL1632 is variable on a timescale of months and it is a promising candidate for a much more accurate time-delay measurement.

6.7.2 GL1838

The raw light curves and the smoothed light curves for GL1838 are presented in Figures 6-4 and 6-17. It is immediately clear that component B is much noisier than component A. This agrees with the data from the GL1838 ATCA monitoring campaign by Winn et al. [16]. Given the fact that the images formed by this gravitational lens contain only compact components, we expect to observe a negligibly small constant flux term⁹ Therefore, we expect any fractional flux variation in image A to match the fractional flux variation in image B. The observation that the light curve of Image B is much noisier than that of Image A, suggests that we are observing Galactic scintillation. However, the radiation from image B passes through an arm of the spiral lensing galaxy. This radiation encounters large volumes of plasma and Image B is scatter-broadened. In this situation, the image angular size becomes too large to be affected by scintillation. This hypothesis could be tested by measuring the angular dimensions of images A and B using VLBA, since VLA cannot resolve the individual component of GL1838.

⁹Remember, constant flux terms come from extended structures.

The predicted time delay, $h\Delta\tau$, is on the order of tens of days (depending on the exact lensing galaxy model) [12]. The ATCA monitoring campaign provided relatively flat light curves for GL1838 and the data did not allow Winn et al. to measure the time delay. In our campaign, the GL1838 light curves varied very slowly. The light curve of image A rises at the end of Season 2, and the same feature can be seen in the light curve of image B.

I was not able to reliably measure the time delay using the quadratic weighting method for Pelt's dispersion calculations. This was due to the large light curve scatter of image B (see Figure 6-4). However, it was possible to measure a tentative time delay by uniformly weighting all the points in the dispersion calculation. The resulting D_1^2 curve, shown in Figure 6-18, has a minimum at $\tau_{min} = 40$ days, which is in roughly good agreement with the predictions of a simple lens model [14]. Figure 6-19 shows the composite light curve formed by combining light curves of images A and B. Note that the image B light curve was scaled in magnitude and shifted back in time by 40 days. I used a 3-point median smoothing filters for image A in order to avoid smoothing the rise at the end of second season. I had to use a 9-point filter for image B because it contained significant scatter.

Monte Carlo simulations, which require quadratic weighting, did not provide support for a time delay of ~ 40 days. The simulations were plagued by the fact that the B light curve was very noisy. I estimated the uncertainty of the proposed time delay graphically, using the dispersion plot in Figure 6-18. I identified $\tau_{left} = 30$ days and $\tau_{right} = 40$ days as the lower and upper limits of this measurement. Thus, for GL1383 I propose a tentative time delay of $\tau_{AB} = 35 \pm 5$ days. Another monitoring campaign is necessary to confirm or reject this tentative measurement.

6.7.3 GL2004

The final light curves and smoothed light curves for GL2004 are shown in Figures 6-5 and 6-20. Similarly to GL1838, one of the light curves is considerably noisier than the other. The flux density ratio of components A and B is approximately 1:1 for GL2004, I suppose that GL2004 is subject to differential scintillation. In other words,

component A scintillates more than component B. This monitoring campaign did not observe the lens often enough to sample the scintillation process.

Although the initially predicted time delay for GL2004 was on the order of days, the fact that the lensing galaxy is a spiral complicates the situation. Due to the uncertainties in the lens model, the potential time delay could range from a few days to a few tens of days [32]. The standard lens model predicts that image B lags behind image A [13].

My simulation results, presented in Figure 6-21, show that Pelt's algorithm fails to measure the time delay of GL2004. This is due to the excessive amount of noise in the light curve of component A, which masks any real variation that might have occurred. Our observations also show that this lens is variable on very long timescales. The slow variability of GL2004, combined with the fact that image A is very noisy makes it challenging to measure the GL2004 time delay in a future monitoring campaign.

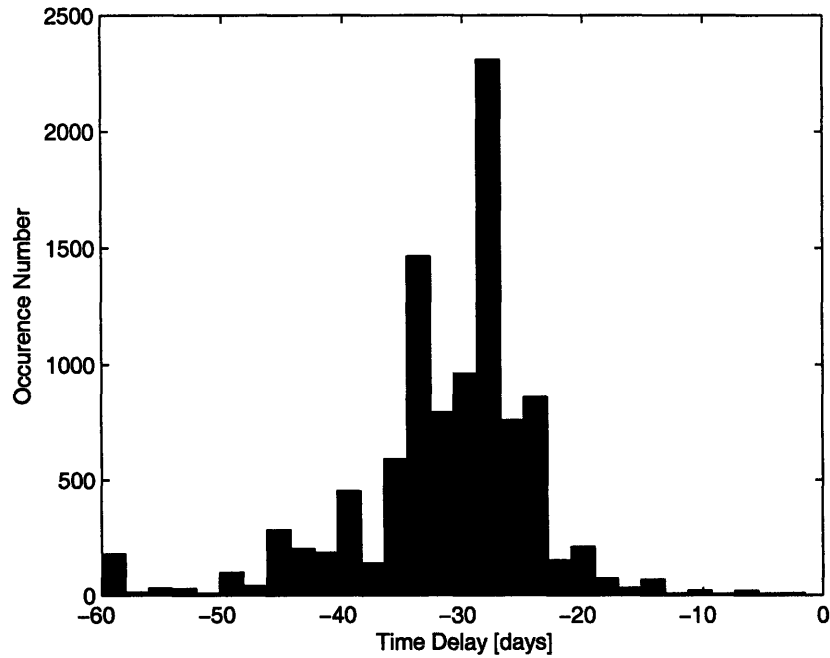


Figure 6-9: GL1608: The results of 10000 simulations using Fassnacht's data from Season 1 [7]. The simulated light curves were generated as described in the Simulation subsection. The calculated time delay is $\tau_{AB} = -30^{+4}_{-7.5}$ days (68% confidence interval). This time delay is negative because image B leads image A. This is in good agreement with the result $\tau_{AB} = -31^{+3}_{-2}$ days (68% confidence interval) calculated by Fassnacht using the same data. Note that Fassnacht used different smoothing filters and a somewhat different Monte Carlo procedure.

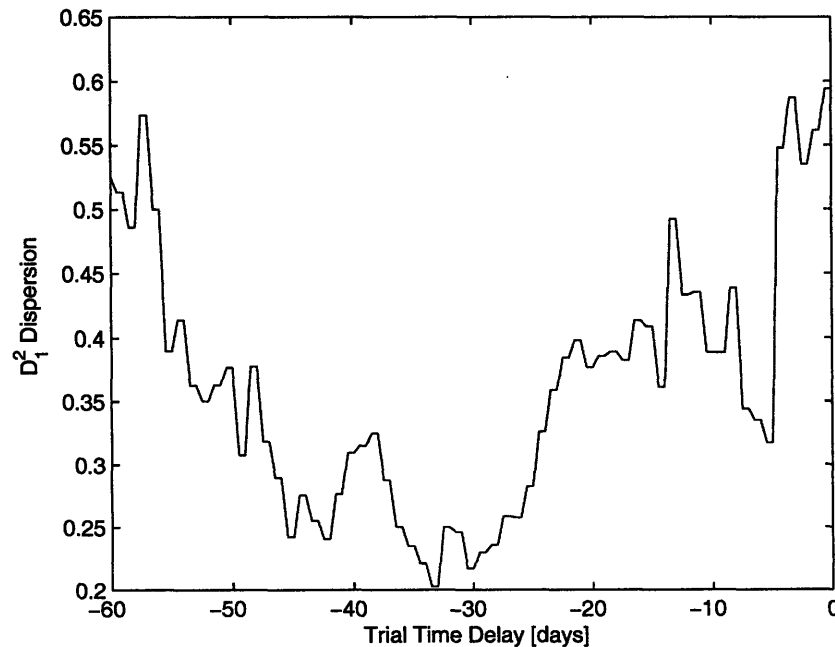


Figure 6-10: GL1608: Dispersion plot for Fassnacht's Season 1 data. Quadratic weighting was used to calculate D_1^2 dispersion.

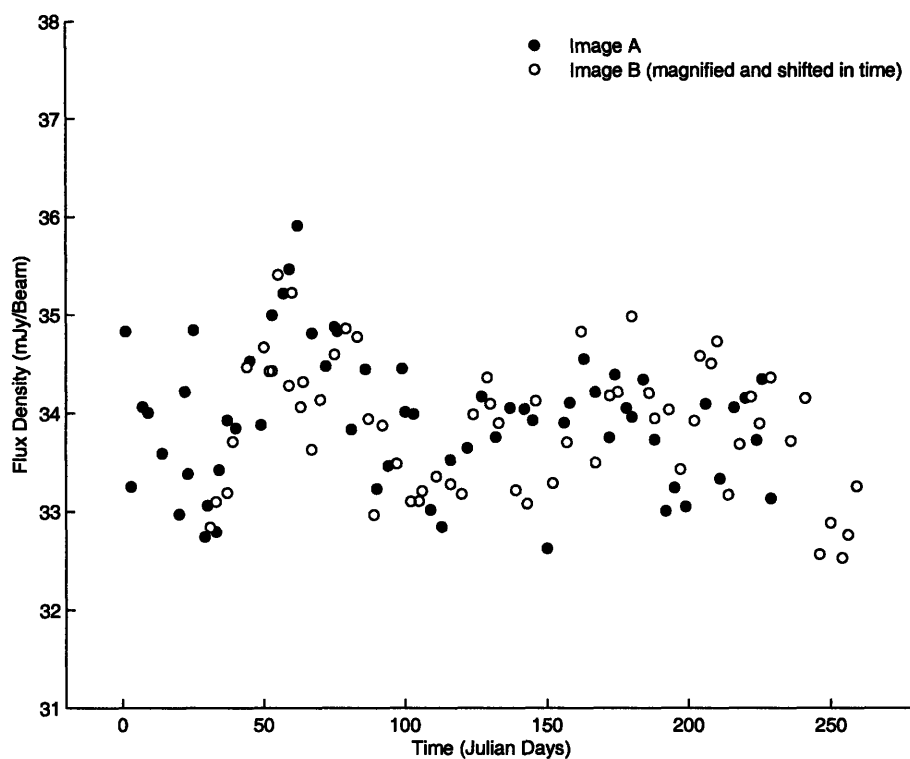


Figure 6-11: GL1608: Combined Final Light-Curve. Based on Fassnacht's data and parameters calculated by my code.

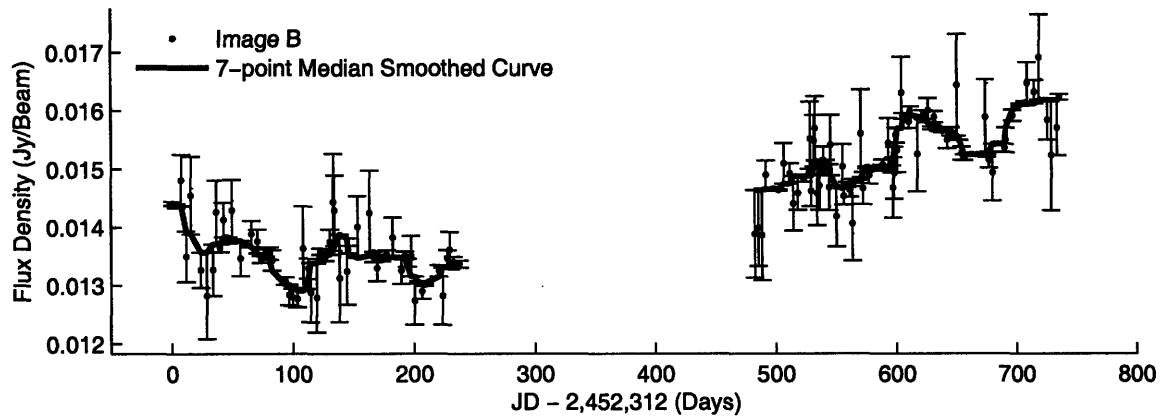
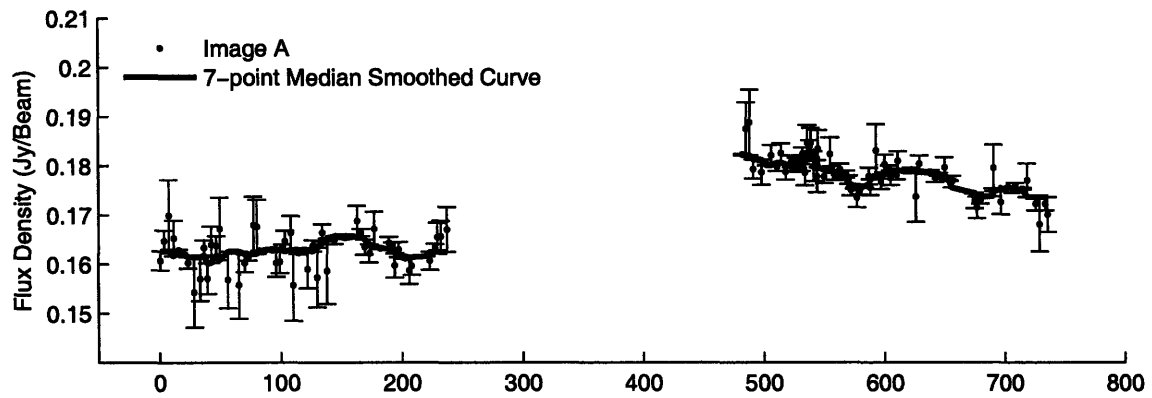


Figure 6-12: GL1632: Smoothed light curves. Fractional flux variations are the same in both images.

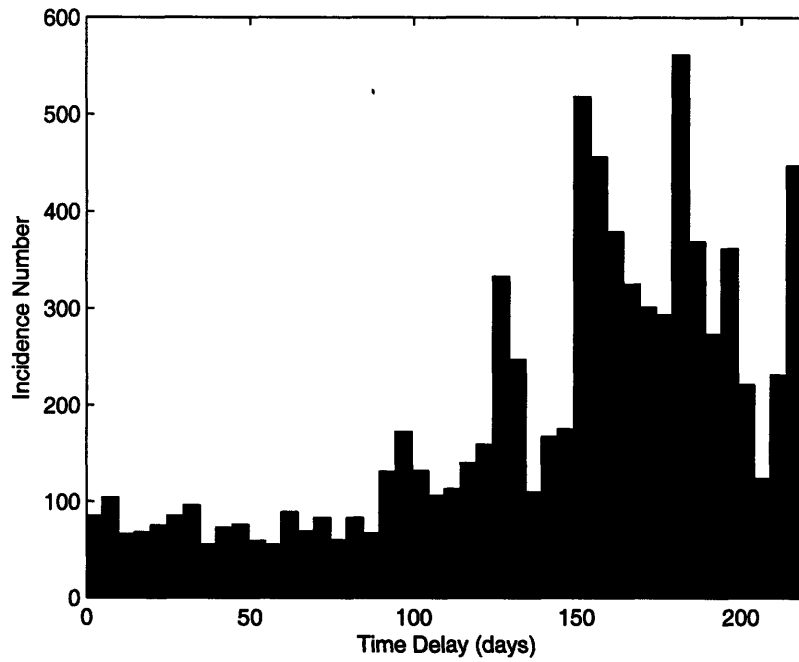


Figure 6-13: GL1632: Histogram showing the results of 10000 simulations. This histogram suggests a tentative time delay $\tau_{AB} = 156^{+38}_{-70}$ days. Note that this is a very conservative estimate.

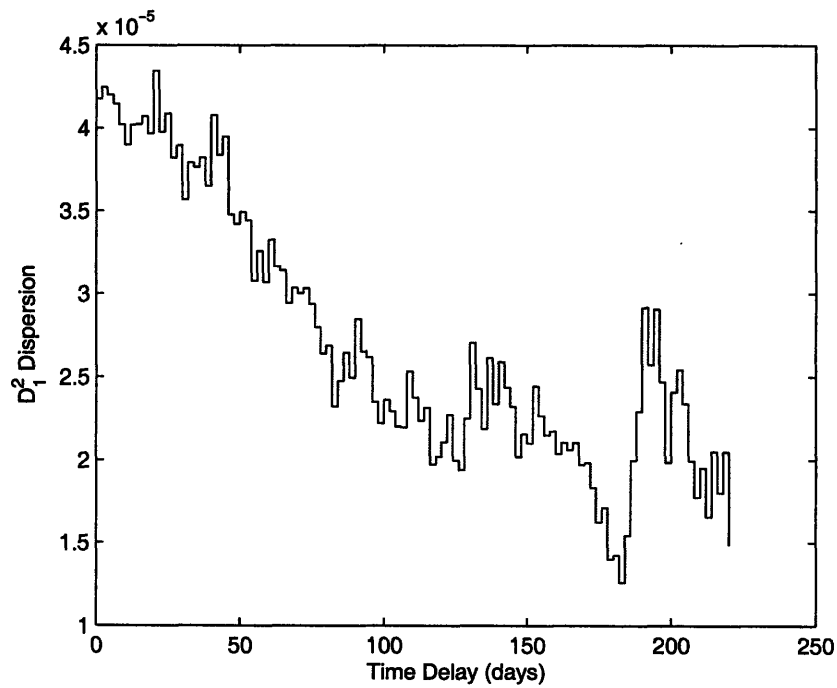


Figure 6-14: GL1632: Dispersion curve for optimal fit parameters. $M_1 = 12.156$ and $M_2 = 11.340$ are the best-fit magnification ratios for Seasons 1 and 2.

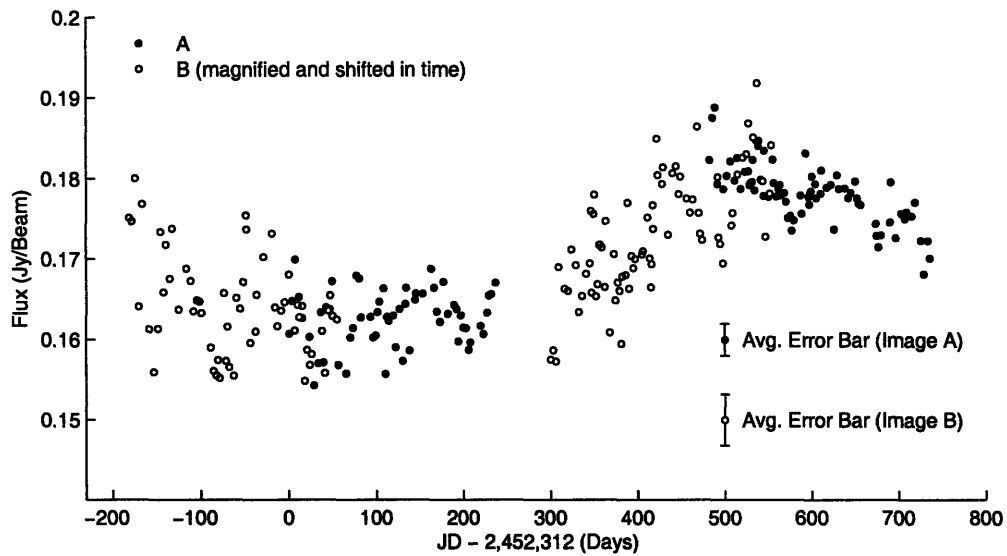


Figure 6-15: GL1632: Combined Light Curve for $M_1=12.156$ and $M_2=11.340$ and a time delay of $\tau_{AB} = 182$ days, corresponding to the minimum in the Pelt Dispersion plot form Figure 6-14

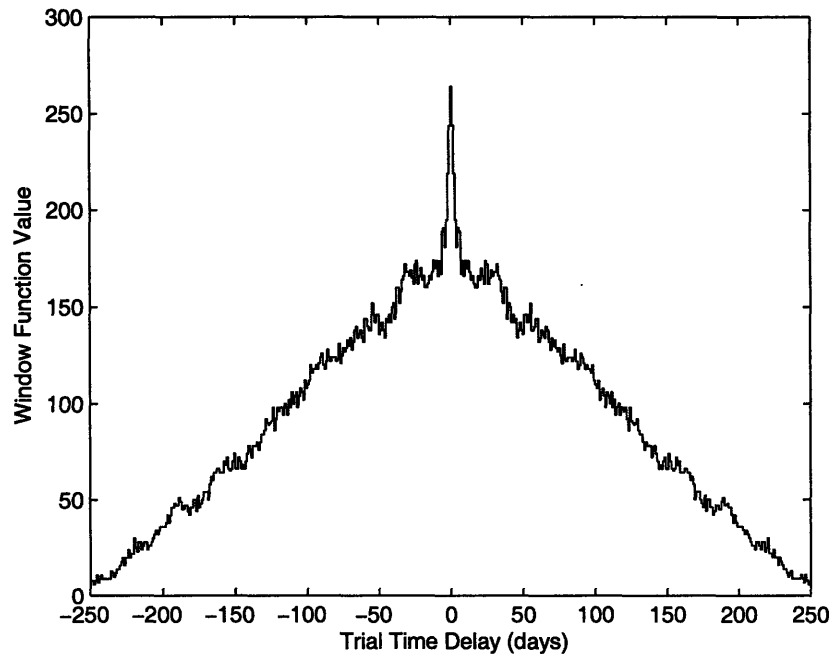


Figure 6-16: GL1632: Window function versus trial time delays. The window function value corresponds to the number of pairs of points contributing to the dispersion calculation. As the trial time delay increases, the curves are shifted more with respect to each other, the overlap between light curves of A and B decreases, and the window function value goes down.

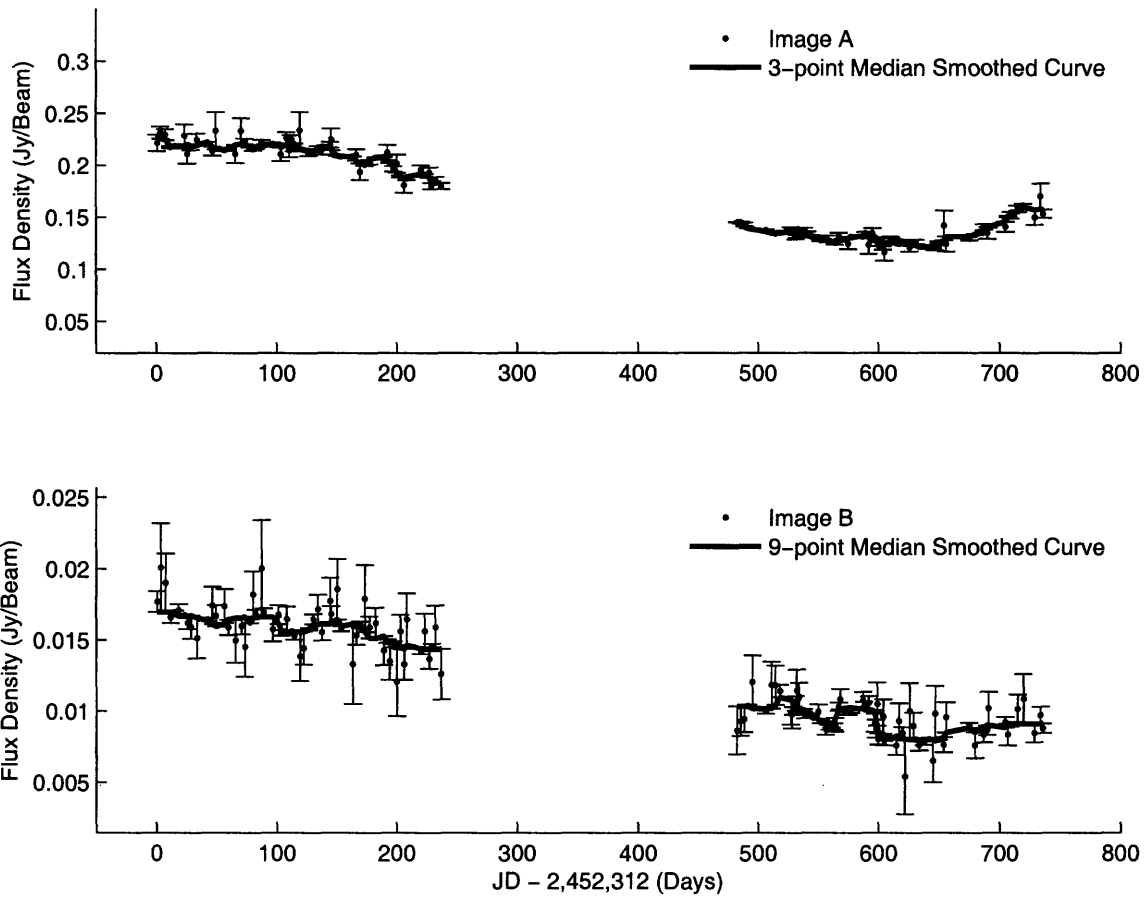


Figure 6-17: GL1838: Smoothed light curves. Fractional flux variations are the same for images A and B. Note that the light curve of image B is much noisier than that of image A.

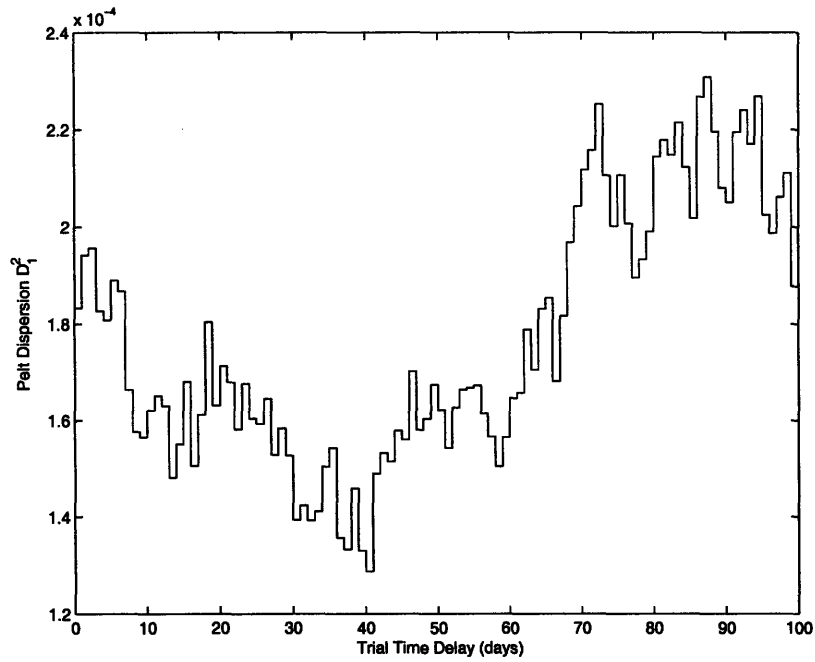


Figure 6-18: GL1838: Plot of Pelt D_1^2 dispersion as a function of trial time delays (all light-curve points were weighted uniformly). This plot suggests a time delay $\tau_{AB} = 40$ days. The best fit magnification ratios are $M_1=13.68$, and $M_2=14.04$ for Seasons 1 and 2 respectively. See Figure 6-19 for the combined light curves.

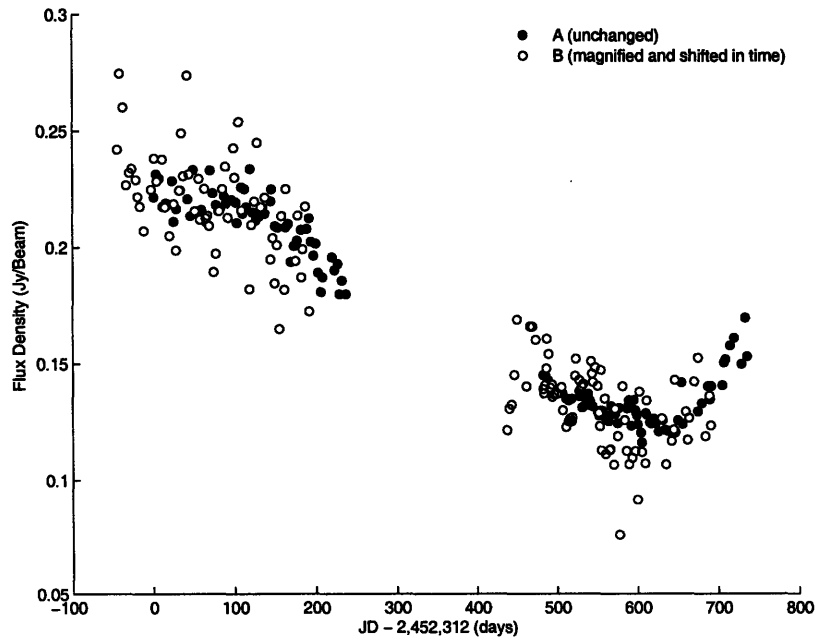


Figure 6-19: GL1838: Combined light curves for $M_1=13.68$, $M_2=14.04$, and $\tau_{AB} = 40$ days

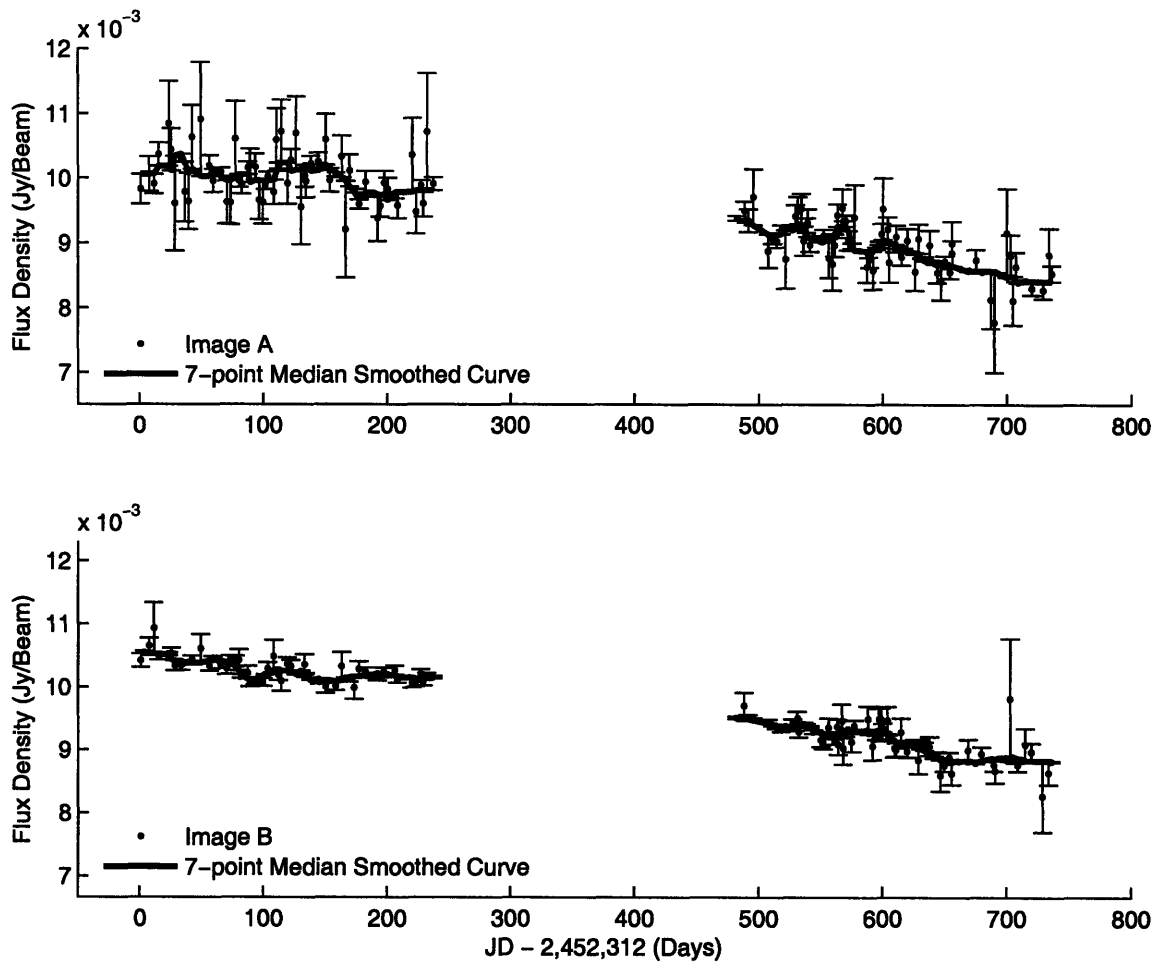
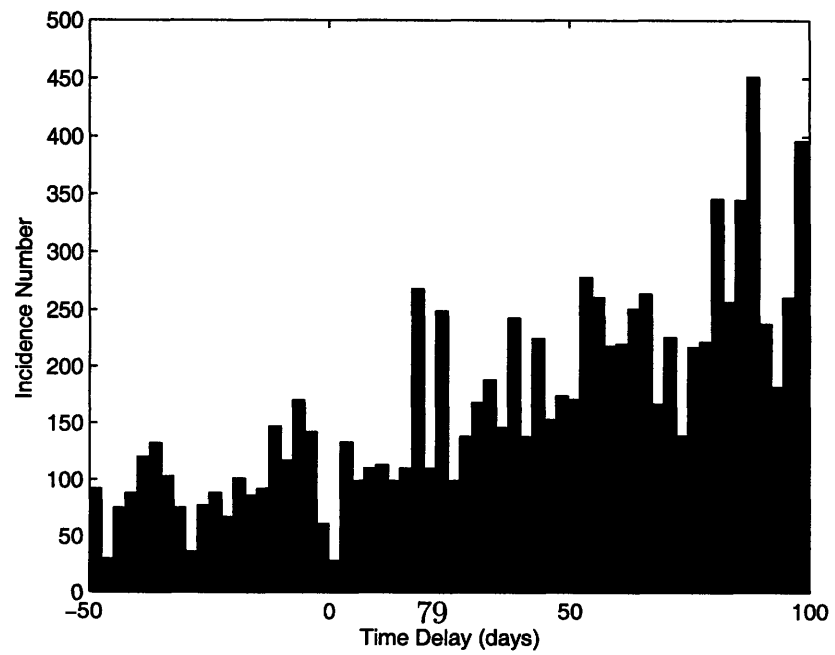


Figure 6-20: GL2004: Smoothed light curves. Fractional flux variations are the same on both plots. Note that the light curve of image A is much noisier than that of image B.



Chapter 7

Conclusions

In this undergraduate thesis, I present data obtained during two seasons of gravitational lens monitoring. The campaign observed five gravitational lenses: GL1608, GL1830, GL1632, GL1838, and GL2004 from 24 January 2002 until 18 September 2002, and from 21 May 2003 until 29 January 2004.

Prof. J. N. Winn scheduled the campaign and acquired the data, I reduced and analyzed it. I started with the raw FITS files and finished with the finalized light curves for all monitored sources. I analyzed the light curves in an attempt to measure the time delays for three gravitational lenses – GL1632, GL1838, and GL2004.

GL1830 was dropped from the time-delay analysis because I used an oversimplified model for the lens images, a model that did not account for extended emissions. Another gravitational lens, GL1608, was dropped from the time delay analysis because it was monitored for only for the first 2/3 of Season 1, and its light curves contained very little variation.

The data reduction cycle was comprised of flagging and primary flux calibration in AIPS, followed by secondary flagging and source model fitting in DIFMAP. Final light curve analysis was done in MATLAB. I wrote various Bash and PERL scripts to manage several thousand files generated in the process. I resorted to Monte Carlo simulations in order to check the reliability of my time delay measurements and estimate the uncertainties of these calculations. I analyzed the final light curves of three gravitational lenses using the non-interpolative dispersion method devised by

Pelt et al. [33].

GL1632 showed significant flux variations in both seasons. My analysis suggests a time delay of $\tau_{AB} = 182^{+8}_{-30}$ days for GL1632. The time delay uncertainty associated with this measurement is quite large because of the relatively short duration of VLA monitoring seasons.

Based on these preliminary results, I strongly recommend that GL1632 is monitored continuously for at least 400-500 days in a future campaign. We have already seen that GL1632 is highly variable on timescales of 10^2 days, so it should be possible to accurately measure its time delay in the future.

GL1838 light curves exhibited a very significant flux density variation (50% decrease from Season 1 to Season 2) during our monitoring campaign. Unfortunately, this massive variation occurred very slowly and steadily over approximately 650 days. Our observations suggest that GL1838 is variable on very long timescales, which makes it difficult to measure the time delay. My analysis suggests a tentative GL1838 time delay measurement of $\tau_{AB} = 35 \pm 5$ days.

GL2004 light curves exhibited mild variability on long timescales. The smoothed light curves show some small features on timescales of tens of days. Due to the large intrinsic scatter in the light curve of image A, I suspect that the short-time-scale features are not real. Differential scintillation is the most plausible explanation for the large scatter in image A of GL2004. Pelt's dispersion method combined with Monte Carlo simulations failed to measure the time delay of GL2004.

Based on our observations, I expect that it will be challenging to measure the GL2004 time delay (given the low amplitude of flux variations and the long time scale of these variations). The fact that the light curve of image A has a large scatter, perhaps due to differential scintillation, makes it even more difficult to accurately measure the time delay of this lens.

I would like to make a crude estimate of H_0 using the tentative time delays for GL1632 and GL1838. For GL1632, Winn et al. published a predicted time delay $h\Delta t = 118.5 \pm 1.9$ days¹ for a flat cosmological model with $\Omega_m = 0.3$, $\Omega_\Lambda = 0.7$

¹Recall that $h = H_0/100$ km sec⁻¹ Mpc⁻¹.

[15]. This prediction is based on a singular isothermal spherical model for the lensing galaxy. Using Winn’s model and my measurement of $\tau_{GL1632} = 182_{-30}^{+8}$ days, I calculated $H_0 = 65.1_{-2.7}^{+12.9}$ km sec⁻¹ Mpc⁻¹.

For GL1838, Winn et al. used a singular isothermal ellipsoid lensing galaxy model to predict a time delay of $h\Delta t = 14.9 \pm 0.2$ days for a flat cosmological model with $\Omega_m = 0.3$, $\Omega_\Lambda = 0.7$. Using my tentative time delay measurement of $\tau_{GL1838} = 35 \pm 5$ days, I calculated $H_0 = 42.6_{-5.3}^{+5.1}$ km sec⁻¹ Mpc⁻¹.

7.1 What Could Have Been Done Differently

A significant amount of observing time was dedicated to the secondary flux calibrators. We convinced ourselves that secondary calibrators were necessary only as a means of correcting the gain elevation effect. Since the VLA data center started automatically applying gain elevation correction sometime in late 2002, it was unnecessary to observe secondary calibrators in Season 2.

In addition, it would have been more advantageous to have an uninterrupted monitoring campaign. This would have allowed us to measure the GL1632 time delay more accurately. It is impossible to have continuous VLA campaigns because of its regular configuration changes². However, it should be possible to have continuous monitoring campaigns with the VLBA, which does not change configuration³.

I mentioned that I used an oversimplified model of GL1830 for fitting FITS data in DIFMAP. This was suggested by the fact that the flux density of GL1830 images varied when the VLA configuration changed. If more time were available, I would have created a more sophisticated source model that would have accounted for the extended emission and the faint Einstein ring.

²For such a campaign, we can only use the A, BnA, and B VLA array configurations.

³There is a major problem with VLBA, it has a large of angular resolution, and it is much harder to find compact sources that could serve as calibrators.

7.2 Future Work

This monitoring campaign acquired most of the data in the X-band (8.5 GHz) and some GL2004 data was acquired in VLA's C-band (5 GHz). For my thesis, I focused mainly on the X-band data. Sometime within the next three months I intend to reduce the C-band data. Combined with the X-band data, it could be used to study the scintillation in GL2004.

It would be also interesting to measure the angular dimensions of GL1838 components A and B with VLBA and investigate the possibility of differential scintillation.

I also intend to repeat GL1830 source fitting in DIFMAP. This will be more challenging because the model will have to account for a faint Einstein Ring and some extended structure.

Finally, I intend to summarize the results of this work and publish them in a joint paper with Professor J. N. Winn.

Appendix A

AIPS and DIFMAP Scripts

This appendix contains a few AIPS, DIFMAP, and Bash shell scripts that I used to process the VLA monitoring data. In addition to these, I used a variety of customized Bash shell scripts for file management, but the scripts presented here did most of the "heavy lifting" for data reduction.

A.1 "Do-It-All" AIPS Script

```
#####  
$ This AIPS script was used for data flagging and primary flux calibration $  
$ The dollar sign denotes the beginning of a comment string $  
#####  
  
$ This procedure defines a few variables used throughout the script  
#####  
proc defvar  
  string*12 utdate; $ Name of the current epoch, for example "AW576.020124"  
  scalar TEMP; $ Temporary reference antenna,  
finish  
  
$ This Procedure loads the raw file corresponding to epoch "utdate"  
$ Use command "loadraw('AW576.020124')"  
$ RAWDATA is a BASH environment variable denoting the folder where  
$ raw data files are stored. A sample filename is "AW576.020124.FG.UVF"  
#####  
proc loadraw(utdate)  
  task 'fitld';  
  infile 'RAWDATA:' !! utdate !! '.FG.UVF';  
  outname utdate; outdisk 0; outclass 'XBAND'; outseq 0;  
  optype 'UV'; ncount 1; dotable 1; douvcomp 1; doconcat -1;  
  go fitld; wait;
```



```

uvrange 0 200;
go calib; wait;

calsour ''; uvrange 0;
calsour(1)='1545+478';
calsour(2)='1734+094';
calsour(3)='2130+050';
calsour(4)='2355+498';
calsour(5)='1820-254';
calsour(6)='1651+014';
calsour(7)='2011-157';
calsour(8)='1642+689';
go calib; wait;

task 'getjy';
sources '';
sources(1)='1400+621';
sources(2)='1634+627';
sources(3)='1545+478';
sources(4)='1734+094';
sources(5)='2130+050';
sources(6)='2355+498';
sources(7)='1820-254';
sources(8)='1651+014';
sources(9)='2011-157';
sources(10)='1642+689';
calsour '1734+094',''; qual -1; calcode '';
bif 1; eif 0; timer 0; anten 0; subarray 0;
selband -1; selfreq -1; freqid -1; snver 0;
go getjy; wait;

task 'clcal';
sources ''; soucode ''; calsour ''; calcode ''; qual -1;
timer 0; subarray 0; anten 0; selband -1; selfreq -1;
freqid -1; opcode 'cali'; interpol '2pt'; intparm 0;
smotype ''; snver 0; gainver 2; gainuse 3;
refant TEMP ;
go clcal; wait;
priority 0; prnumber 0; prttask ''; prtime 0;
docrt -1;
outprint 'FOLDER_!!substr(utdate,7,12)!!':'!!utdate!!'.CLCALMSG';
go prtmsg;

task 'split';
sources(1)='1400+621';
sources(2)='1634+627';
sources(3)='1545+478';
sources(4)='1734+094';
sources(5)='2130+050';
sources(6)='2355+498';
sources(7)='1820-254';
sources(8)='1651+014';
sources(9)='2011-157';
sources(10)='1642+689';

```



```

modelfit 3;
selfcal fa,fa,0.5;
modelfit 3;

!Print the residual map RMS
print imstat(rms);
print "Measuring RMS for AMOD";
wmod 'amodfile';

!Print the status of the job
print "Done with file ", inpfiler, ".";

!End of DIFMAP Script

```

A.3 Bash Script for Screening Calibrators in DIFMAP

```

#!/bin/bash
#####
# Script used to screen a single epoch and look at all calibrators      #
# I use it to write down the antennas that need to be reflagged in AIPS #
# This script helps get perfect flagging for the calibrators           #
# Use: > CALscreen_an_epoch.sh AW576.020124                            #
#####

CAL_LIST="/thesis/DIFMAP_DATA/list_of_calibrators.txt";
CALIBRATORS='cat $CAL_LIST';
DIR="/thesis/DIFMAP_DATA";
EPOCH=$1; #ex: "AW576.020124"
DATE=${1:6:6}; #ex: "020124"

for CAL in $CALIBRATORS;
do
    FILE=$DIR/$DATE/$CAL.$EPOCH.UVF;

    if [[ -f "$FILE" ]] && [[ ! -z 'cat $FILE' ]];
    then

echo "Opening file: $FILE";
difmap <<HERE
observe $FILE;
mapunit arcsec;
select i;
device /xs;
radpl;
!tplot;
HERE

echo "Done with file: $FILE";
    else
        echo "$FILE is empty or does not exist";
    fi;
done;
# End of BASH script

```

A.4 Bash Script for Flagging GLs in DIFMAP

```
#!/bin/bash
#####
# This script is used to screen and flag Gravitational lens data in DIFMAP #
# Note that this script writes to disk a new file with flagged GL data      #
# Use: > GLscreen_an_epoch.sh AW576.020124                                  #
#####

GL_LIST="/thesis/DIFMAP_DATA/list_of_gls.txt";
GLS='cat $GL_LIST';
DIR="/thesis/DIFMAP_DATA";
EPOCH=$1; #ex: "AW576.020124"
DATE=${1:6:6}; #ex: "020124"

for GL in $GLS;
do
    FILE=$DIR/$DATE/$GL.$EPOCH.UVF;

    if [[ -f "$FILE" ]] && [[ ! -z 'cat $FILE' ]];
    then
echo "Opening file: $FILE";

difmap <<HERE
observe $FILE;
mapunit arcsec;
select i;
device /xs;
radpl;
wobs $DIR/$DATE/$GL.$EPOCH.FG.UVF;
HERE
echo "Done with file: $FILE";
    else
        echo "$FILE is empty or does not exist";
    fi;
done;
# End of Bash script
```

Bibliography

- [1] Taylor G. B.; Carilli C. L.; Perley R. A. *Synthesis Imaging In Radio Astronomy II*. Astronomical Society of the Pacific Conference Series, Volume 180, 1999.
- [2] Einstein Albert. Lens-like action of a star by the deviation of light in the gravitational field. *Science*, (84):506–507, 1936.
- [3] Friedman Alexander. Uber die krummung des raumes (english translation in: Gen. rel. grav. 31 (1999), 1991-2000). *Z. Phys.*, (10):377–386, 1922.
- [4] Ramesh Narayan; Matthias Bartelmann. Lectures on gravitational lensing. A Series of Lectures, Unpublished, May 2006.
- [5] Dyson F. W.; Eddington A. S.; Davidson C. A determination of the deflection of light by the sun's gravitational field, from observations made at the total eclipse of may 29, 1919. *Philosophical Transactions of the Royal Society of London*, (220):291–333, 1920.
- [6] Shepherd M. C. Difmap: An interactive program for synthesis imaging. *Astronomical Data Analysis Software and Systems VI, ASP Conference Series*, 125, 1997.
- [7] C. D. Fassnacht et al. A determination of H_0 with the class gravitational lens B1608+656. I. time delay measurement with the vla. *The Astrophysical Journal*, (527):498–512, December 1999.
- [8] C. D. Fassnacht et al. A determination of H_0 with the CLASS gravitational lens B1608+656. III. a significant improvement in the precision of the time delay measurements. *The Astrophysical Journal*, (581):823–835, December 2002.
- [9] Courbin F. et al. Image deconvolution of the radio ring pks 1830-211. *The Astrophysical Journal*, 499:L119–L123, 1998.
- [10] Fassnacht et al. 1608+656: A gravitationally lensed poststarburst radio galaxy. *The Astrophysical Journal*, 460:L103, 1996.
- [11] Freedman W. L. et al. Final results from the hubble space telescope key project to measure the hubble constant. *The Astrophysical Journal*, 553:47–72, 2001.

- [12] J. N. Winn et al. PMN J1838-3427: A new gravitationally lensed quasar. *The Astronomical Journal*, (120):2868–2878, December 2000.
- [13] J. N. Winn et al. A nearly symmetric double-image gravitational lens. *The Astronomical Journal*, (121):1223–1231, March 2001.
- [14] J. N. Winn et al. PKS J1830-211: A face-on spiral galaxy lens. *The Astrophysical Journal*, (575):103–110, August 2002.
- [15] J. N. Winn et al. PMN J1632-0033: A new gravitationally lensed quasar. *The Astronomical Journal*, (123):10–19, January 2002.
- [16] J. N. Winn et al. The radio variability of the gravitational lens PMN J1838-3427. *The Astronomical Journal*, (128):2696–2703, December 2004.
- [17] Jauncey D. L. et al. An unusually strong einstein ring in the radio source pks1830211. *Nature*, 352:132–134, July 1991.
- [18] Kochanek et al. The fundamental plane of gravitational lens galaxies and the evolution of early-type galaxies in low-density environments. *The Astrophysical Journal*, 543:131–148, November 2000.
- [19] Lidman C. et al. The redshift of the gravitationally lensed radio source pks 1830-211. *The Astrophysical Journal*, 514:L57–L60, 1999.
- [20] Lovell J. E. J. et al. The time delay in the gravitational lens pks 1830-211. *The Astrophysical Journal*, 508:L51–L54, 1998.
- [21] Myers et al. 1608+656: A quadruple-lens system found in the class gravitational lens survey. *The Astrophysical Journal*, 447:L5–L8, July 1995.
- [22] Snellen et al. Radio observations of the quadruple lens 1608+656. *The Astrophysical Journal*, 447:L9–L12, July 1995.
- [23] C. D. Fassnacht and G. B. Taylor. Compact symmetric objects as radio flux density calibrators. *Astronomical Journal*, 122:1661–1668, Sep 2001.
- [24] Zwicky Fritz. Nebulae as gravitational lenses. *Physical Review*, (51):290–290, 1937.
- [25] Zwicky Fritz. On the probability of detecting nebulae which act as gravitational lenses. *Physical Review*, (51):679–679, 1937.
- [26] A. S. Cohen; J. N. Hewitt; C. B. Moore; D. B. Haarsma. Further investigation of the time delay, magnification ratios, and variability in the gravitational lens 0218+357. *The Astrophysical Journal*, (545):578–590, December 2000.
- [27] Edwin Hubble. A relation between distance and radial velocity among extragalactic nebulae. *Proceedings of the National Academy of Sciences of the United States of America*, 15(3):168–173, 1929.

- [28] Hogbom J. Aperture synthesis with a non-regular distribution of interferometer baselines. *Astrophysical Journal Supplement Series*, 15:417–426, 1974.
- [29] Rao Pramesh A.; Subrahmanyam R. *MNRAS*, 231:229, 1988.
- [30] Sjur Refsdal. The study of quasi-stellar objects and distant galaxies. *MNRAS*, 295(128), 1964.
- [31] W. H. Press; G. B. Rybicki. Magnification ratio of the fluctuating light in gravitational lens 0957+561. 1999.
- [32] J. N. Winn; P. B. Hall; P. L. Schechter. Mass and dust in the disk of a spiral lens galaxy. *The Astrophysical Journal*, (597):672–679, November 2003.
- [33] J. Pelt; W. Hoff; R. Kayser; S. Refsdal; T. Schramm. Time delay controversy on qso 0957+561 not yet decided. *Astronomy and Astrophysics*, (286):775–785, 1994.
- [34] Refsdal Sjur. Possibility of determining distances and masses in lensing systems. *MNRAS*, 295(134), 1966.